Prominent in vivo influence of single interneurons in the developing barrel cortex

Yannick Bollmann, Laura Modol, Thomas Tressard, Artem Vorobyev, Robin Dard, Sophie Brustlein, Ruth Sims, Imane Bendifallah, Erwan Leprince, Vincent de Sars, et al.

nature neuroscience

Article

https://doi.org/10.1038/s41593-023-01405-5

Prominent in vivo influence of single interneurons in the developing barrel cortex

Received: 7 June 2020

Accepted: 13 July 2023

Check for updates

Yannick Bollmann[1,6], Laura Modol[1,6], Thomas Tressard[1,6], Artem Vorobyev[1], Robin Dard[1], Sophie Brustlein[1], Ruth Sims[2], Imane Bendifallah[2], Erwan Leprince[1], Vincent de Sars[2], Emiliano Ronzitti[2], Agnès Baude[1], Hillel Adesnik[3,4], Michel Aimé Picardo[1], Jean-Claude Platel[1], Valentina Emiliani[2], David Angulo-Garcia[5,6] & Rosa Cossart[1,6]

Spontaneous synchronous activity is a hallmark of developing brain circuits and promotes their formation. In this study, ex vivo, synchronous activity was shown to be orchestrated by a sparse population of highly connected GABAergic 'hub' neurons. The recent development of all-optical methods to record and manipulate neuronal activity in vivo now offers the unprecedented opportunity to probe the existence and function of hub cells in vivo. Using calcium imaging, connectivity analysis and holographic optical stimulation, we show that single GABAergic, but not glutamatergic, neurons influence population dynamics in the barrel cortex of non-anaesthetized mouse pups. Single GABAergic cells mainly exert an inhibitory influence on both spontaneous and sensory-evoked population bursts. Their network influence scales with their functional connectivity, with highly connected hub neurons displaying the strongest impact. We propose that hub neurons function in tailoring intrinsic cortical dynamics to external sensory inputs.

Spontaneous synchronous activity is a universal process by which developing neuronal networks adjust their cell numbers, mature single-cell morpho-physiological properties and form and prune synapses[1,2]. This ultimately allows for the emergence of an internal topographically organized representation of external sensory inputs, enabling the active exploration of the world and opening a period of experience-dependent circuit refinement[3]. Spontaneous synchronous activity is generated by the interaction between local circuit dynamics and bottom-up inputs[1,2,4]. As such, it is proposed to function in calibrating and patterning local circuits to the statistics of the external world and in coordinating the timing of their intrinsic maturational programs to environmental influences[2].

Although their prevalence and importance are indisputable, the circuit mechanisms by which these spontaneous synchronous activity patterns emerge are only starting to be elucidated. In addition to cellular excitability, synaptic efficacy and inhibition/excitation balance, network connectivity is a critical determinant of synchronous neuronal activity. This has been shown in vitro, where most developing neurons contribute to the active cell population, but only a small minority of highly connected (HC) hub cells critically function in coordinating neuronal activation[5,6].

The term 'hub' originates from the theoretical field of complex networks. In networks displaying a heavy-tailed connectivity degree distribution, hubs are the most connected minority (typically the 5% most connected) among a poorly connected majority. This theoretical definition has been translated and applied experimentally to the analysis of neuronal circuits[7]. There, the term 'operational hub' defines a neuron not only displaying a high functional connectivity

[1]Aix Marseille Univ, Inserm, INMED, Turing Center for Living Systems, Marseille, France. [2]Wavefront-Engineering Microscopy Group, Photonics Department, Vision Institute, Sorbonne University, INSERM, CNRS, Paris, France. [3]Department of Molecular & Cell Biology, University of California, Berkeley, Berkeley, CA, USA. [4]Helen Wills Neuroscience Institute, University of California, Berkeley, Berkeley, CA, USA. [5]Departamento de Matemáticas y Estadística, Facultad de Ciencias Exactas y Naturales, Universidad Nacional de Colombia, Manizales, Colombia. [6]These authors contributed equally: Yannick Bollmann, Laura Modol, Thomas Tressard, David Angulo-Garcia, Rosa Cossart. e-mail: rosa.cossart@inserm.fr

degree (that is, a functional hub) but also actively involved in network synchronization, the stimulation of which single-handedly impacts spontaneous synchronous activity. Combining online calcium data analysis and single-cell interrogation using patch-clamp recordings, we previously identified operational hub neurons in hippocampal slices at the end of the first postnatal week (p)[5]. Hippocampal hub neurons were GABAergic, displayed a widespread axonal arbor and originated from the earliest stages of embryogenesis[8]. Experimental evidence for hub neurons was also obtained in entorhinal cortex slices[6], suggesting that hub cells may be a shared connectivity motif within developing cortical networks and, as such, critical players in circuit maturation.

Despite this potentially major role, it remains unknown whether hub cells orchestrate network bursts in the intact brain. This is an important issue because spontaneous activity in the developing cortex is driven mostly by sensory feedback, an active input that is not present in slices[9,10]. It is, therefore, essential to test the existence and function of hub neurons while maintaining the integrity of sensory inputs, even more because the polarity of GABAergic transmission may be affected by slicing[11]. Addressing this important question requires recording and manipulating neuronal activity in vivo at cellular resolution, which has been, until recently, an experimental challenge.

The recent development of computational algorithms to infer functional connectivity based on activity patterns and of all-optical approaches to achieve these tasks in vivo[12–15] (using shaped light and soma-restricted opsins) now open the unique opportunity to precisely manipulate the activity of hub cells in the intact brain of awake pups. In this stuidy, we used calcium imaging, online connectivity analysis and two-photon holographic optical stimulation to dissect the functional connectivity schemes giving rise to synchronized activity in the barrel cortex of non-anaesthetized mouse pups and to disentangle the relative contributions of excitatory and inhibitory neurons in such phenomena and the role of sensory inputs in setting up local connectivity motifs.

We show here that single GABAergic neurons can exert a significant inhibitory influence on spontaneous and sensory-evoked population bursts as compared to their glutamatergic partners. The network influence of single interneurons scales with their functional connectivity degree, with high input degree hubs controlling spontaneous activity and high output ones controlling the response to whisker stimulation (WS). GABAergic hubs emerge after the end of the first postnatal week, as the density of functional connections among interneurons increases. Such developmental evolution is impaired by sensory deprivation. GABAergic hub cells are, therefore, central communication nodes between local developing circuits and sensory signals.

Results

Postnatal evolution of functional connectivity in developing circuits of the barrel cortex in vivo

We used two-photon microscopy to track the evolution of the functional organization of barrel cortex circuits in developing mouse pups in vivo during the first 2 weeks of postnatal life. We tailored the choice of opsin, calcium reporter and illumination methods to minimize the crosstalk between the actuator and reporter and to maximize stimulation efficiency and cellular resolution; this was even more challenging at early stages of development when cells are densely packed and highly active in a synchronous manner. To this aim, we designed a custom-built setup with two laser sources and used GCaMP6s as a calcium reporter combined with patterned holographic stimulation[16,17] of the fast opsin ST-ChroME[14]. The protocols for viral induction of actuator and reporter proteins co-expression were optimized for early postnatal expression (Supplementary Videos 1 and 2 and Extended Data Fig. 1). We focused on the barrel cortex, a widely studied model area, to understand circuit maturation during early stages of development, positioned at the interface between sensory inputs and intracortical circuits. The barrel cortex is also easily accessible for optical imaging throughout all layers from the pia to infragranular layers. Our experiments focused mostly on layers II/III and were performed during the temporal window that spans from the end of anatomical barrel formation in deep layers (p4–5, depending on GCaMP6s expression) to the onset of active whisking (p11)[18]. A field of 600 × 600 μm^2 was imaged at different cortical depths, up to 500 μm below the surface. Data points were pooled into three successive groups (p5–6, p7–9 and p10–11 for all cells in Fig. 1 and p4–6, p7–9 and p10–11 for GABAergic cells in Fig. 2) based on similarity in terms of dynamics revealed by post hoc analysis.

Contours surrounding co-active pixels were automatically detected, as previously described[19,20]. To infer neuronal spiking from calcium fluorescence signals, we used a deep-learning-based tool (CASCADE)[20] (Methods). The first set of experiments was performed in non-anesthetized transgenic mouse pups generated by the crossing of *GAD67*$^{Cre/+}$ males[21] with females of the *Ai14* reporter line[22], in which GABA neurons could be identified by their expressing td-Tomato, a red fluorescent protein (*GAD67*$^{Cre/+}$*;Ai14*; Fig. 1a and Extended Data Fig. 1d). AAV-hSyn-GCaMP6s was injected at p0 to allow for the expression of the calcium reporter protein in all neurons (Fig. 1 and Extended Data Fig. 1d; $n = 18$ *GAD67*$^{Cre/+}$*;Ai14* mice, 43 imaging sessions). The expression of GCaMP6 was stable between p5 and p11 as well as the total number of imaged cells and the proportion of the td-Tomato$^+$ cells expressing the indicator (Extended Data Fig. 1). Among imaged neurons expressing the calcium reporter, 20% were GABA cells, but only about half of the td-Tomato$^+$ neurons (53 ± 1%) expressed GCaMP6s. This value was constant in all age groups (Extended Data Fig. 1).

To describe the developmental changes in the functional organization of barrel circuits in vivo, we first computed the functional output and input connectivity degrees of the active cells based on the pairwise correlation between inferred spikes, as previously done in vitro[5,6]. Through this analysis of temporal correlations, a 'functional output link' directed from neuron A to neuron B was established if the inferred spikes of A significantly preceded those of B (Fig. 1b and Methods). Conversely, if the inferred spikes of A significantly followed those of B, then a 'functional input link' from B to A was set. The functional output or input connectivity degree of a given neuron was the fraction of active cells displaying a functional output or input link with it, respectively.

We next computed the changes in the connection density and the largest connected component (LCC) across postnatal stages. The connection density was calculated using the total number of functional links (both input and output) divided by the number of all possible connections (Fig. 1c and Methods). The LCC was the fraction of mutually reachable active neurons irrespective of the directionality of the links (Fig. 1d and Methods). We found no differences in the connection density across postnatal stages (Fig. 1c). In contrast, we observed a significant increase in the size of the largest connected graph (amount of cells that are functionally integrated into the circuit) at the latest developmental timepoints (p5–6 versus p10–11, $P < 0.05$; Fig. 1d,e).

To better understand the mesoscopic functional organization of these developing circuits, we next analyzed the distributions of both functional output and input connectivity degrees across developmental stages (Fig. 1f, 1 and 2, respectively). To test the overall distribution that best fits the data, we followed a statistical procedure outlined in ref. 23 (Methods). In this way, we could determine whether input and output functional connectivity degrees followed a power law, exponential or log-normal distribution[5,24–27]. We found that both the input and output connectivity degrees were best fitted with a log-normal distribution with the following parameters (output connectivity: mean = 1.01, s.d. = 1.18; input connectivity: mean = 1.04, s.d. = 1.21).

Because inferring connectivity from activity can lead to errors, especially in HC networks[28], we used two additional methods to calculate connectivity among cells to test whether the order of connectivity degree is maintained regardless of the method. Specifically, we used a weighted version of the pairwise correlation between spike trains and transfer entropy as alternative methods. The three methods converged

https://doi.org/10.1038/s41593-023-01405-5

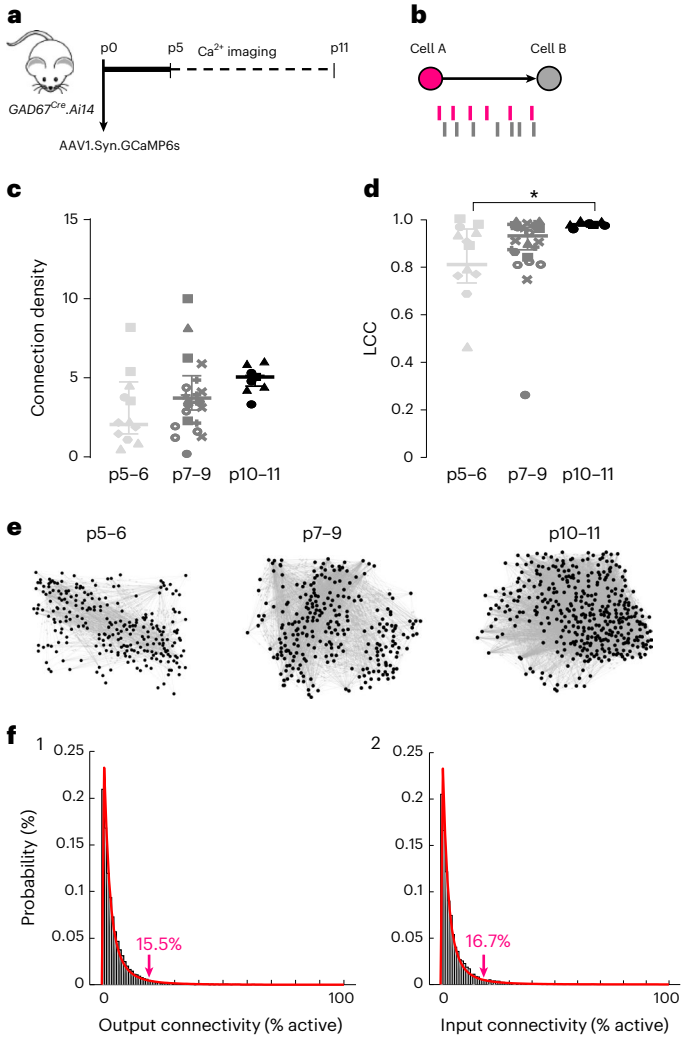

Fig. 1 | Long-tailed distributions define the functional development of the barrel cortex in vivo. a, Schematic representation of the experimental paradigm. Experiments were performed in non-anesthetized GAD67$^{Cre/+}$;Ai14 pups between p5 and p11 (p5–6 $n = 5$ pups (three females and two males), 12 FOVs; p7–9 $n = 9$ (four females and five males), 23 FOVs; p10–11 $n = 3$ (four females and three males), eight FOVs). Pups were injected with AAV1.SynGCaMP6s at p0. In vivo imaging of GCaMP6s and expression of td-Tomato in GAD67$^+$ cells over postnatal development. **b**, Schematic illustration of two functionally connected cells, with the onsets of cell A (pink), always preceding those of cell B (gray), as represented in the schematic raster plot. **c**, Whisker plot indicating the connection density (Methods) as a function of age; Kruskal–Wallis = 2.83; P = NS. **d**, Whisker plot showing developmental evolution of the undirected LCC. Kruskal–Wallis = 7.102; $P = 0.01$. Dunn's post hoc two-sided test shows differences between p5–6 to p10–11 ($P < 0.05$). **e**, Representative graphs showing the LCC from p5 to p11 in vivo. Graphs are constructed based on the pairwise correlation connectivity analysis between the activity onsets of all cells (Methods). Each line (edge) represents an undirected (input or output) connection between nodes. **f**, Probability distribution of output (1) and input (2) functional connectivity degree within all imaged neurons with non-zero connectivity ($n = 11{,}021$ cells for output connections and $n = 10{,}509$ cells for input connections) pooling the three age groups. The data are best fitted using a log-normal distribution (Methods). HC cells are connected to at least 15.5% (output) and 16.7% (input) of all other active cells within the FOV. Box and whiskers correspond to the analysis performed with the mean value of each animal across all recorded FOVs. Each shape corresponds to data points obtained in different mice. Data are given as median and interquartile range.

to a similar rank in connectivity degree, indicating that pairwise correlation is a fair and simple indicator of functional connectivity (Extended Data Fig. 2).

We next focused our analysis on the most connected cells that comprise hub neurons. HC neurons were defined as the 5% most connected active cells, whereas the remaining were termed low connected (LC). We first identified the 5% most connected cells within each age group (HC_{age}). The median output connectivity degree of HC_{age} cells was 17%, 24% and 18% (of active neurons) at p5–6, p7–9 and p10–11, respectively. The median input connectivity degree of HC_{age} cells was 19%, 25% and 21%, respectively. We did not find any significant change with age. Next, we identified the 5% most connected cells (considering output links) across all movies and ages (HC_{global_out}). We observed a similar percentage of HC neurons per imaging session across ages: 4 ± 4% neurons at p5–6 ($n = 12$ fields of view (FOVs)), 7 ± 9% at p7–9 ($n = 23$ FOVs) and 4 ± 1% at p10–11 ($n = 8$ FOVs) (one-way ANOVA: $F_{2,40} = 0.89$; $P > 0.05$). These HC_{global_out} neurons were functionally connected to at least 15% of all active neurons. Similar results were observed for HC_{global_in} neurons (the 5% cells displaying the most input links across all movies and ages): 4 ± 4.0% neurons at p5–6, 7 ± 11% at p7–9 and 4 ± 3% at p10–11 (one-way ANOVA: $F_{2,40} = 0.72$; $P > 0.05$). These HC_{global_in} neurons were functionally connected to at least 17% of all active neurons. In contrast, LC_{global_out} and LC_{global_in} have a median connectivity degree of 1.7% and 1.6%, respectively. Interestingly, we found a significant correlation between the sum of inferred spikes for a given cell (within 1,000 movie frames) and its output and input connectivity degree (adjusted R^2: 0.02, slope: 0.03, $P < 0.0001$; adjusted R^2: 0.06, slope: 0.05, $P < 0.0001$, respectively; Extended Data Fig. 1). This suggests that the more functionally connected cells were also more active.

We conclude that the local functional connectivity between neurons of the developing barrel cortex displays a log-normal distribution comprising HC neurons with most connectivity metrics being independent of age.

GABAergic hub cells functionally connecting interneurons emerge after the first postnatal week in a sensory-dependent manner

Given that GABAergic neurons are more likely to function as operational hubs than their glutamatergic partners in vitro[5], we next focused on their specific contribution to the HC cell population (Fig. 2a). GABAergic cells had a lower median output connectivity degree per FOV than non-GABAergic cells (2% versus 3%, $P < 0.001$; Fig. 2, b1) but a higher median input connectivity degree (5% versus 3%, $P < 0.0001$; Fig. 2, b2). Accordingly, there was a higher proportion of GABAergic neurons within the HC_{global_in} population than the HC_{global_out} population (26% versus 4%). In this way, GABAergic neurons contributed three times more to the HC_{global_in} population than their average proportion within the imaged cell population (8% were td-Tomato$^+$ among active GCaMP6s-expressing neurons). Given this distinct pattern of functional connectivity as well as the brain-wide rise in connectivity within the interneuron population toward the end of the first postnatal week[2], we next investigated more specifically the functional connectivity between GABAergic neurons. Because only half of all GABAergic cells were labeled with the viral strategy used above (53 ± 1% of td-Tomato-expressing neurons co-expressed GCaMP6s, $n = 8$ pups; Extended Data Fig. 1), we generated mice expressing GCaMP6s exclusively in GABA neurons (*GAD67*$^{Cre/+}$;*Ai96* mice) by crossing *GAD67*$^{Cre/+}$ with the reporter line *Ai96* (RCL-GCaMP6s) (The Jackson Laboratory; Fig. 2c). As previously reported, GCaMP6s expression was specific, stable and even as early as p4 (Fig. 2a and Extended Data Fig. 3)[29]. This earlier timepoint was included in the developmental analysis of GABAergic networks. As with Fig. 1, we found that a log-normal distribution best fits the data (output connectivity: mean = 1.52, s.d. = 1.21; input connectivity: mean = 1.44, s.d. = 1.31; Extended Data Fig. 3). This indicates that there is a subset of HC GABAergic interneurons. On average, HC_{out_age} GABA cells (the 5% of GABAergic cells with the highest output connectivity within a given age group) were connected to 16%, 21% and 41% of all active GABAergic cells at p4–6, p7–9 and p10–11,

https://doi.org/10.1038/s41593-023-01405-5

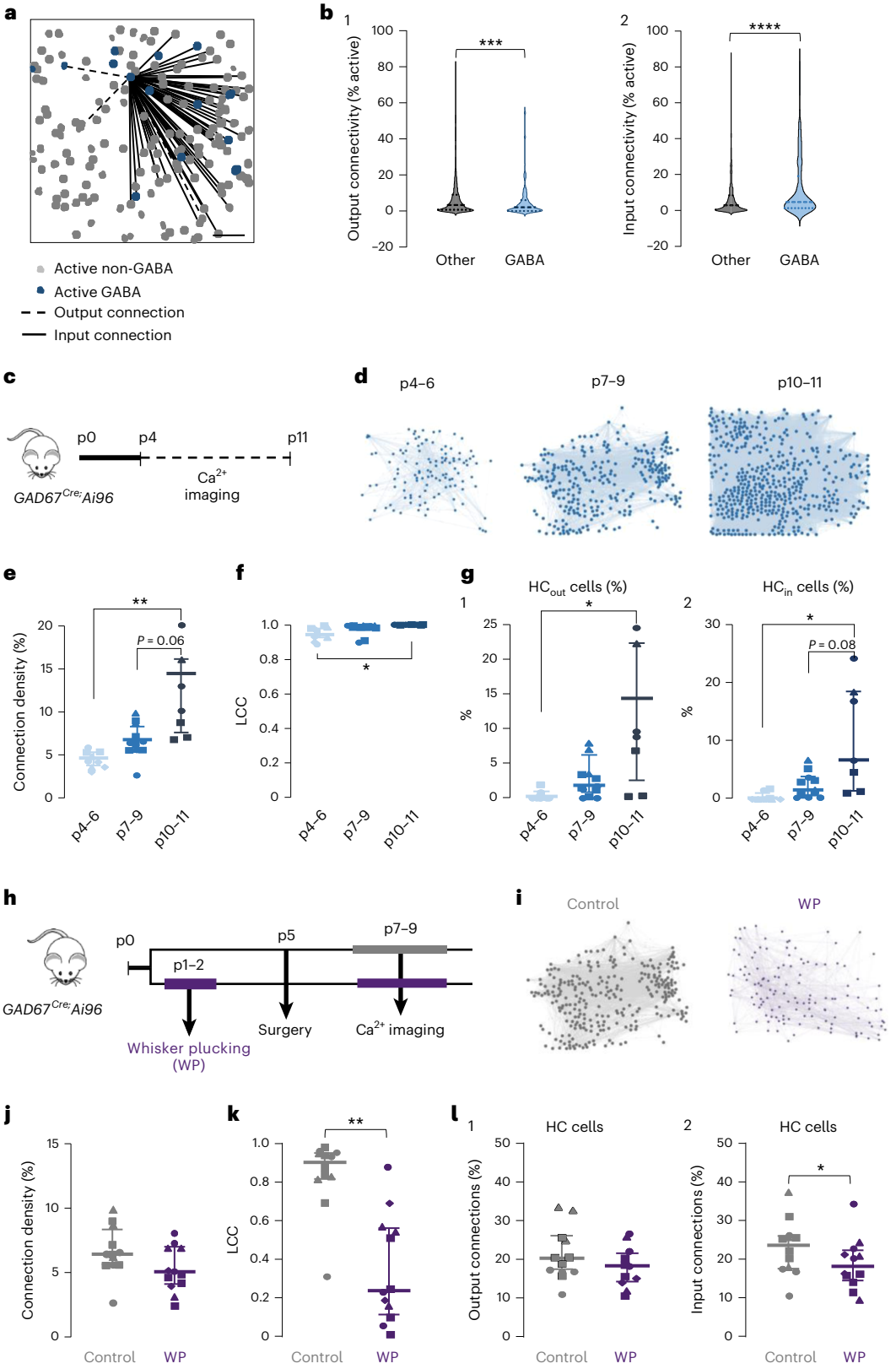

respectively. We observed a similar pattern for HC_{in_age} GABA cells (the 5% of GABAergic cells with the highest input connectivity within a given age group), which were connected to 17%, 22% and 46% of all active GABAergic cells at p4–6, p7–9 and p10–11, respectively. Interestingly, we observed that both HC_{global_out} and HC_{global_in} GABAergic cells were anatomically closer than non-HC GABAergic cells ($P < 0.0001$; Extended Data Fig. 3).

In contrast to what we described in Fig. 1, the interneurons with the highest connectivity expand their functional domains as age progresses, eventually connecting almost half of the other interneurons by p10–11. Consequently, the connection density within the interneuron population significantly increased between p4–6 and p10–11 ($P < 0.01$; Fig. 2d,e). Additionally, we observed an increase in the size of the LCC (see above) between p4–6 and p10–11 ($P < 0.05$; Fig. 2e,f). This notable

https://doi.org/10.1038/s41593-023-01405-5

Fig. 2 | Development of functional connectivity among GABAergic neurons. **a**, Contour map of active cells in a representative imaging session at p7–9 (active non-GABA (gray), active GABA cells (blue filled)). Each edge represents a connection (continued line represents input connections and dotted lines represent output connections). Scale bar, 100 µm. **b**, Violin box plots indicating the output (1) and input (2) connectivity of all cells (gray) and GABAergic cells (blue). Two-sided Mann–Whitney test: $F_{2,40}$ = output connectivity: $U = 134{,}951$; $P = 0.0004$; input connectivity: $U = 129{,}161$; $P < 0.0001$. **c**, Schematic representation of the experimental paradigm. Experiments were performed in non-anesthetized GAD67Cre-Ai96 pups between p4 and p11: p4–6 $n = 4$ (three females and one male), nine FOVs; p7–9 $n = 3$ (one female and two males), 12 FOVs; and p10–11 $n = 3$ (two females and one male), seven FOVs. Data are given as median and interquartile range. **d**, Representative functional graphs showing the undirected LCC from p4 to p11 in vivo. Graphs are constructed based on the pairwise correlation connectivity analysis between the activity onsets of all cells (Methods). Each line (edge) represents a directed (input or output) connection between nodes. **e**, Whisker plot indicates significant changes in the connection density across postnatal stages. One-way ANOVA $F_{2,7} = 8.636$; $P = 0.01$. Tukey's (two-sided) post hoc comparison indicates differences between p4–6 and p10–11 ($P < 0.01$) and a tendency between p7–9 and p10–11 ($P = 0.06$). **f**, LCC also shows significant changes according to age. One-way ANOVA $F_{2,7} = 4.95$; $P < 0.05$. Tukey's (two-sided) post hoc comparison indicates differences between p4–6 and p10–11 ($P = 0.05$). Data are given as median and interquartile range. **g**, Whisker plots indicate the fraction of HC cells in terms of output (1) and input (2) as a function of age according to the calculated HCglobal. GABA HC cells emerge during the second postnatal week. (1) % HCout_age: Kruskal–Wallis = 6.704; $P = 0.01$. Dunn's (two-sided) post hoc comparison indicates differences between p4–6 and p10–11 ($P < 0.05$). (2) % HCin_age: Kruskal–Wallis = 7.043; $P < 0.01$. Dunn's (two-sided) post hoc comparison indicates differences between p4–6 and p10–11 ($P < 0.05$) and a tendency between p7–9 and p10–11 ($P = 0.06$). **h**, Schematic representation of the experimental paradigm. Experiments were performed in non-anesthetized GAD67Cre-Ai96 pups between p7 and p9 ($n = 4$ pups, 12 FOVs). **i**, Representative graphs showing the LCC at p7–9 in a control and deprived pup (WP). Each line (edge) represents an undirected (input or output) connection between nodes. **j**, Whisker plot indicates a tendency to significance in the connection density between control and WP animals. Two-sided t-test: $t(22) = 1.83$; $P = 0.08$. **k**, Whisker box plot indicates differences in the size of the LCC (undirected graph) between control and WP animals. Mann–Whitney (two-sided) test (U) = 25; $P = 0.005$. **l**, Whisker plot shows differences of the 95th percentile of median output percentage of connections of the 5% most connected cells for output (1) and for input (2) connections. (1) Mann–Whitney (two-sided) test (U) = 52; P = NS. (2) Mann-Whitney test (U) = 43; $P = 0.050$. Box and whiskers correspond to the analysis performed with the mean value of each animal across all recorded FOVs. Each shape corresponds to data points obtained in different mice. Data are given as median and interquartile range. NS, not significant.

evolution was mirrored by a significant increase in the fraction of HC_{global} GABAergic cells as a function of age. Hence, the fraction of HC_{global_out} and HC_{global_in} cells significantly increased between p4–6 and p10–11 ($P < 0.05$; Fig. 2g, 1 and 2). Consequently, GABAergic networks become more densely connected with age, with a notable transition occurring after the first postnatal week, when both the number and degree of GABA hubs connecting other interneurons (both input and output) significantly increase, becoming functionally connected to almost half of the other interneurons.

Because the rise in connectivity among GABAergic neurons is known to be dependent on sensory inputs, we next investigated whether the prominent change in the functional organization of GABAergic networks described above was preserved in sensory-deprived mice. To this aim, *GAD67*$^{Cre/+}$;*Ai96* pups were sensory deprived by plucking the whiskers (WP) for 2 d after birth as previously described[30] (Fig. 2h–l j). This manipulation showed a tendency to impact the increase in the connection density (Fig. 2j; $P = 0.08$) and significantly altered the increase in the size of the LCC (Fig. 2k,i; $P < 0.01$) already at p7–9. This indicates a general decrease in network connectivity after sensory deprivation. Accordingly, we found that the connectivity degree of HC_{in} (but not HC_{out} GABA) cells significantly decreased in WP conditions when compared to control ($P = 0.05$; Fig. 2l). We conclude that the rise in functional connectivity within GABAergic neurons at the end of the first postnatal week is partly dependent upon early sensory inputs.

Single GABAergic neurons de-synchronize spontaneous network bursts

Considering that a high functional connectivity degree does not necessarily imply a high effective connectivity, we next attempted to identify which of these HC neurons were operational hub cells—that is, cells that modify network dynamics when activated. To this aim, we co-expressed the fast soma-targeted opsin ST-ChroME[14] together with GCaMP6s in *GAD67*$^{Cre/+}$ or *Emx1*$^{Cre/+}$ mice (to restrict opsin expression to GABAergic or glutamatergic cells) (Fig. 3, a1, b1, a2, b2 and Extended Data Fig. 4). In vitro current-clamp recordings were

Fig. 3 | Targeted holographic stimulation of GABAergic but not glutamatergic neurons in vivo impacts spontaneous network activity. Schematic representation of the experimental paradigm performed in non-anesthetized GAD67$^{Cre/+}$ pups ($n = 11$ (seven females and four males), 26 stimulated cells) (**a**) and in Emx1$^{Cre/+}$ pups ($n = 10$ (five females and five males), 28 stimulated cells) (**b**) between p7 and p11. (1) Animals were injected at p0 with AAV1.hSyn.GCaMP6s.GFP and AAV9.CAG.DIO.ChroME-ST.mRuby3. (2) In vivo imaging of GCaMP6s and ChroME. Contour map of all active cells with the targeted HC GABAergic (**a**2) and glutamatergic (**b**2) cell (pink) and arrows indicating its functional (outputs and input) links. Scale bar, 100 µm. Twenty-six GABAergic and 28 glutamatergic neurons were stimulated in total. (3) Visual example of the effect of single GABAergic (**a**3) and glutamatergic (**b**3) stimulation on network activity. A cell was qualified as influencing network dynamics if the median value of the order parameter during simulation significantly differed ($P < 0.0001$, Wilcoxon rank-sum test) from baseline and post-stimulation, whereas baseline and post-stimulation values did not. Upper panels show the representative raster plot for each example indicating the inferred spikes as a function of time, corresponding to the three recorded periods: baseline, stimulation (stim, pink) and post-stimulation. Middle panel (global activity) indicates the sum/mean of all active cells within the FOVs throughout the three recorded periods. Bottom panels (order parameter) show calculated variations in the synchronization of network activity (Methods). (4) Differences in the order parameter between the stimulation period and the baseline period as a function of the functional connectivity of the stimulated GABAergic (**a**4) and glutamatergic (**b**4) cells (gray). Panels indicate the correlation with either output (OUT) or input (IN) connectivity degree for the GABA (**a**4, OUT: two-sided t-test, $P = 0.37$; IN: two-sided t-test, $P = 0.01$) or the glutamatergic (**b**4, OUT: two-sided t-test, $P = 0.79$; two-sided t-test, IN: $P = 0.18$) cells. Cells that had a significant impact on network synchronization (measured as order parameter) are highlighted in pink. Of the 26 GABAergic single-handled stimulated cells, eight impacted network activity (**a**4). Among all stimulated glutamatergic cells ($n = 28$), only one significantly affected spontaneous calcium events (**b**4). We found a significant correlation between the input connectivity degree of GABAergic cells and the strength of the modulation of the Kuramoto order parameter ($P = 0.012$). (5) Effective connectivity heat map measured as the time-lagged cross-correlation difference (normalized cross-correlation difference) between pre-stimulation and post-stimulation periods (3.7 s) between the GABAergic (**a**5) and glutamatergic (**b**5) stimulated cell and all other active cells within the FOV. The stimulated cells are outlined in pink. Negative values indicate that the cross-correlation was higher after stimulation (blue). Positive values indicate that cross-correlation was higher before stimulation (red). Stimulation of a single GABAergic cell has a larger impact on the activity on other cells in the network. **c**, Quantification of the effect of single-cell stimulation (as measured in **a**5 and **b**5), pooled from all FOVs. Two-sample two-sided Kolmogorov–Smirnov test ($P < 0.0001$).

https://doi.org/10.1038/s41593-023-01405-5

performed to probe the reliability and efficiency of the light-induced cell response at early postnatal development (Extended Data Fig. 5). We found that spiking was reliably triggered in both GABAergic and glutamatergic ST-ChroME-expressing neurons for 10-Hz and 40-Hz stimulation protocols using wide-field visible light (Extended Data Fig. 5).

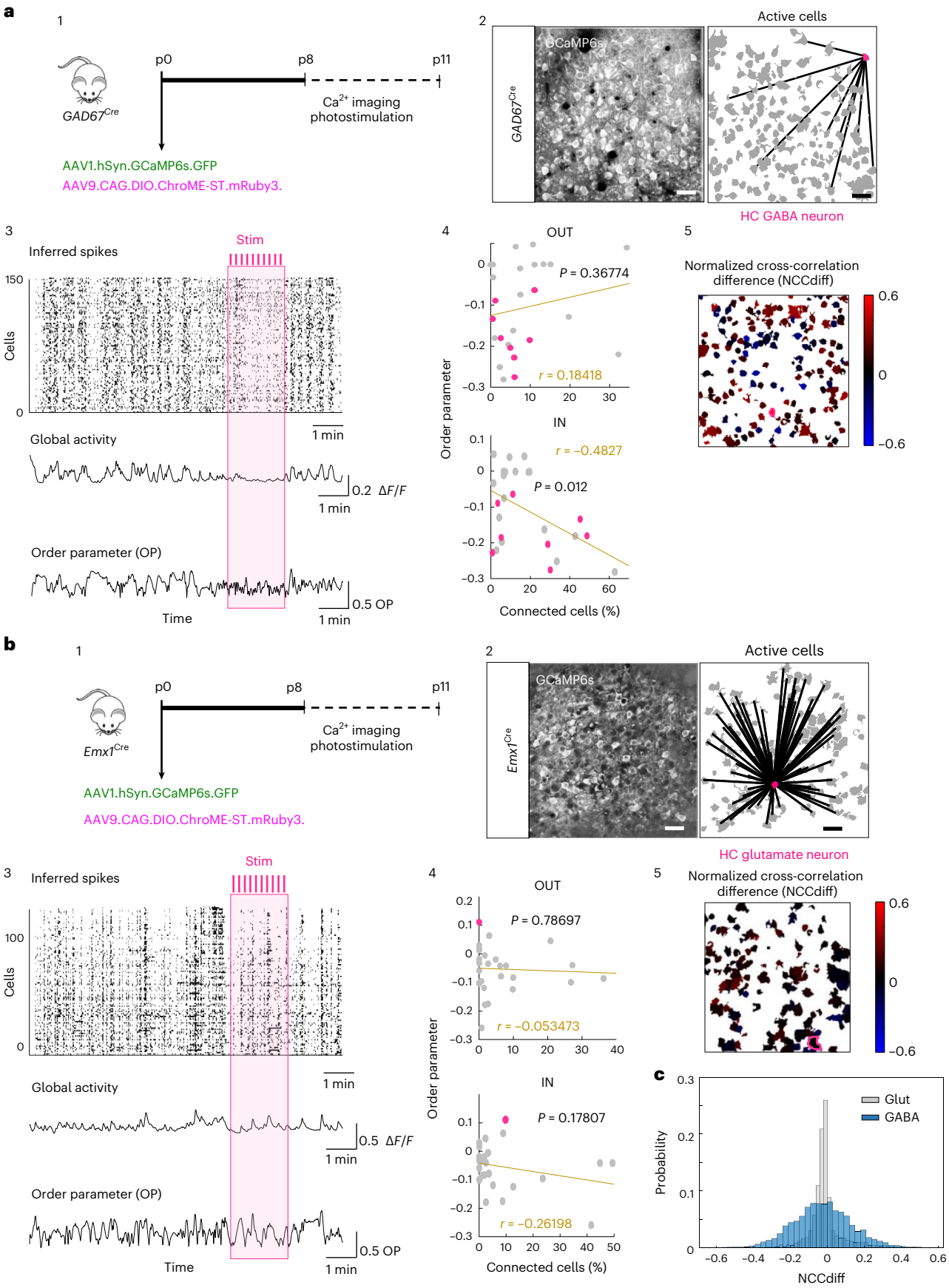

For in vivo experiments, functional connectivity was computed online from the 5-min-long baseline movies before the 100-s-long stimulation period. The stimulation was achieved using two-photon holographic stimulation in a custom-built setup (Methods) and consisted of 10 light pulses of 10-ms duration and 10-µm spot size, delivered at 10 Hz or 40 Hz, every 10 s with a power of 0.3–0.5 mW µm^{-2}. This was followed by a recovery period (that is, no stimulation). Such illumination conditions have been demonstrated to ensure reliable spike generation in vivo[31]. Calcium imaging was performed in an FOV of 350 × 350 µm^2, scanned at 2.7 Hz, with 2-µs dwell time per pixel (0.68 µm per pixel). These illumination conditions were sufficient to keep the artifactual depolarization associated with the activation of opsin-expressing neurons by the imaging lasers below 5 mV[31]. Cells targeted for photostimulation displayed a significant calcium transient time-locked to the stimulation (Extended Data Fig. 6a for GABA and Fig. 6b for glutamatergic cells). We controlled that the stimulation light pulses did not cause per se abnormal cell activation by targeting GCaMP6-expressing cells that did not express the opsin in vivo (n = 12 cells and n = 3 animals; Extended Data Fig. 7). No significant calcium fluorescence signal was evoked by light pulses in these cells (Extended Data Fig. 7).

We next probed the impact of single-cell stimulation on spontaneous neuronal dynamics (Fig. 3 and Methods). Figure 3a,b provides a visual overview of the changes in population activity (inferred spikes and global activity) and synchronization (Kuramoto order parameter). A stimulated neuron was classified as significantly modulating spontaneous network synchronization if the median value of the Kuramoto order parameter was significantly different between baseline and stimulation and returned to the baseline value during recovery. This measure was calculated by extracting the firing phase of each cell in time and computing the modulus of the averaged complex number $e^{i\theta(t)}$ across all cells (Methods). A Kuramoto order parameter close to 1 indicates highly synchronized activity, whereas a value close to 0 is an indicator of asynchronous behavior. We found that 31% (eight of 26) of the 26 stimulated GABAergic cells significantly modulated network synchronization (n = 26 FOVs, 11 pups; Fig. 3, a3, and Supplementary Video 1), but only 3% (one of 28) of the 28 stimulated glutamatergic cells (n = 28 FOVs, 10 pups; Fig. 3, b3, and Supplementary Video 2). The net observed effect of stimulation of a single GABAergic neuron was a decrease in the Kuramoto order parameter (that is, less synchrony). Interestingly, the strength of this modulation increased with input connectivity degree (Fig. 3, a4), whereas no systematic relationship was observed for glutamatergic cells (Fig. 3, b4). Therefore, we found operational input hubs among GABAergic cells. To further characterize the impact of single-cell stimulation on the activity of other cells in the network, we next examined the difference in time-lagged cross-correlation between the stimulated cell and all other cells in the FOV centered on the time of stimulation. In agreement with the observed change in the Kuramoto order parameter for GABAergic cells compared to glutamatergic cells, we found that GABAergic cells exert a significantly stronger modulation on the activity of other cells time-locked to the stimulation (Fig. 3, a5, b5, c5; P < 0.0001). Therefore, using network analysis to predict the net influence of single neurons according to their topological embedding, we show that highly connected GABA neurons function in suppressing activity and limiting synchronization.

GABAergic hub cells influence the response of local circuits to sensory inputs

Sensory inputs transmitted to the neocortex by the thalamus are critically involved in triggering early network synchronization[1]. Notably, GABA neurons may serve as early transient relays of such thalamic inputs to the neocortex[32,33]. We next asked whether single HC GABA neurons could function in relaying sensory inputs to intracortical circuits (Fig. 4). Whiskers were stimulated with air puffs while imaging (Fig. 4a). To this aim, we performed holographic suppression of GABAergic neurons using co-expression of the fast soma-targeted inhibitory opsin ST-GtACR[14] together with GCaMP6s in *Lhx6*$^{Cre/+}$ mice (Fig. 4a,b). *Lhx6*$^{Cre/+}$ mice label GABAergic neurons originating from the medial ganglionic eminences (MGE), which account for about 70% of all cortical interneurons[34]. Targeted ST-GtACR1-expressing cells displayed a significant decrease in calcium transients time-locked to the photoinhibition protocol using both in vitro current-clamp recordings in *Lhx6*$^{Cre/+}$ ST-GtACR1-expressing cells (Extended Data Fig. 8) and in vivo two-photon holographic inhibition (continuous suppression of activity for five frames locked to the whisker stimulation (WS) 0.3-0.5 mW µm^{-2}, on a spot size of 10 µm) (Methods and Extended Data Fig. 9). Calcium imaging was performed as detailed above for the photoactivation experiments, which kept the artifactual hyperpolarization of opsin-expressing neurons during calcium imaging below 2 mV. The final number of analyzed cases was 43 (n = 43 photo-inhibited cells and n = 8 animals).

We first asked whether the response of imaged neurons to WS reflected their functional connectivity degree. To this aim, we calculated, for all active cells, the change in their calcium onset frequency during WS relative to control. We found a significant correlation between this relative activity change during WS and functional connectivity degrees (both input and output) in most FOVs (n = 43). Interestingly, the correlation coefficients found with input degrees were generally positive, indicating an increase in firing during WS, whereas negative correlation coefficients were found in the case of output degrees, indicating a decrease in firing during WS (Fig. 4c). Therefore, input and output connectivity orthogonally determines whether cells will increase or decrease their firing during WS as compared to baseline (Extended Data Fig. 10b).

Fig. 4 | GABAergic neurons convey WS to local circuits. a, Schematic representation of the experimental paradigm. Photoinhibition experiments and imaging sessions were performed in non-anesthetized Lhx6$^{Cre/+}$ pups at p7 and p9 (n = 7 (five females and three males), 37 inhibited cells) injected with AAV1.hSyn.GCaMP6s.GFP and AAV5.hSyn.SIO.stGtACR-FusionRed at p0. **b**, Representative raster plot indicating inferred spikes as a function of time, showing baseline, WS (orange) and combined WS and single-cell photoinhibition (PI, blue). Red dotted line in the bottom histogram indicates the statistical threshold above which the number of co-active contours exceeds chance levels (99th percentile). **c**, We computed the distribution of the correlation coefficients per FOV (37) of the firing activity, as measured by global calcium activity onsets (Fig. 3, a3 and b3), during WS relative to control and the in-degree and out-degree of imaged cells. Correlations with in-degree led to more positive correlation coefficients (increase in firing rates during WS are positively related with high in-degree), and negative correlations are more related to out-degree (decrease in firing rates during WS are more related with high out-degree, two-sample Kolmogorov–Smirnov test, $P = 1.31 \times 10^{-6}$). **d**, Example of changes in network activity (sum of active cells) during WS and WS paired with photoinhibition of a single Lhx6$^+$ cell. **e**, (1) PSTH of network activity centered around WS, in WS only (orange trace) and WS paired with PI (blue trace). Inlay shows $\Delta F/F$ for all active centered around WS. (2) PSTH of the order parameter centered around WS for both conditions (WS and WS + PI). Traces illustrate the effect after WS, which is an increased burstiness after WS only. **f**, (1) Paired box plot illustrates the maximum of the PSTH (max PSTH) response in WS and WS + PI conditions. Two-sided paired t-test: P = 0.001. (2) Paired box plot illustrating the difference in the maximum values of the PSTH of the order parameter (max order parameter) for WS and WS + PI conditions. Two-sided paired t-test: P = 0.029. **g**, Quantification of **f**showing the correlation between the changes observed in **e** and the output connectivity degree of photoinhibited cells. (1) A significant relationship was observed between changes in the maximum PSTH of the networks' response to WS and the output connectivity degree of the stimulated cell (two-sided t-test: P < 0.001). (2) Similarly, changes in the maximum of the PSTH of the order parameter between WS and WS + PI is significantly related to the output connectivity degree of the stimulated GABAergic cell (two-sided t-test: P = 0.01). Each dot in **e** (1 and 2) and **f** (1 and 2) represents an FOV. Data are presented as median and interquartile range.

https://doi.org/10.1038/s41593-023-01405-5

We last analyzed the effect of single-neuron photoinhibition (Fig. 4d) using two measures (Fig. 4e,d, 1 and 2). We first computed the peristimulus time histogram (PSTH) of calcium onsets centered on WS with and without paired photoinhibition (Fig. 4e, 1, inset) and calculated the average PSTH across cells (Fig. 4e, 1, main, and Methods). Photoinhibition of single interneurons increased the amplitude of the average PSTH peak (Fig. 4f, 1, $P < 0.001$), indicating an increased network response to WS when a single interneuron was inhibited. Second, we computed the value of the average Kuramoto order parameter centered on the time of WS (Fig. 4e, 2) and found that synchronization increased when pairing photo-inhibition and WS (Fig. 4f, 2). This result is in agreement with the increase in the PSTH response previously observed (Fig. 4e, 1, and Fig. 4f, 1), where the larger maximum in the Kuramoto order parameter reflects a higher local synchronization, which is, in turn, a consequence of time-locked cell activity (PSTH responses). Remarkably, we found that the effect of single interneuron stimulation on both metrics (maximum average PSTH and maximum average Kuramoto order parameter) significantly correlated with the output connectivity degree (Fig. 4g, 1 and 2), indicating that single highly functionally connected GABAergic hub neurons are more likely to limit the local network response to sensory stimulation.

Discussion

Using light to read and evoke neuronal activity in vivo, this study reveals how single GABAergic neurons influence network synchronizations in the barrel cortex. Such network impact, mainly inhibitory and

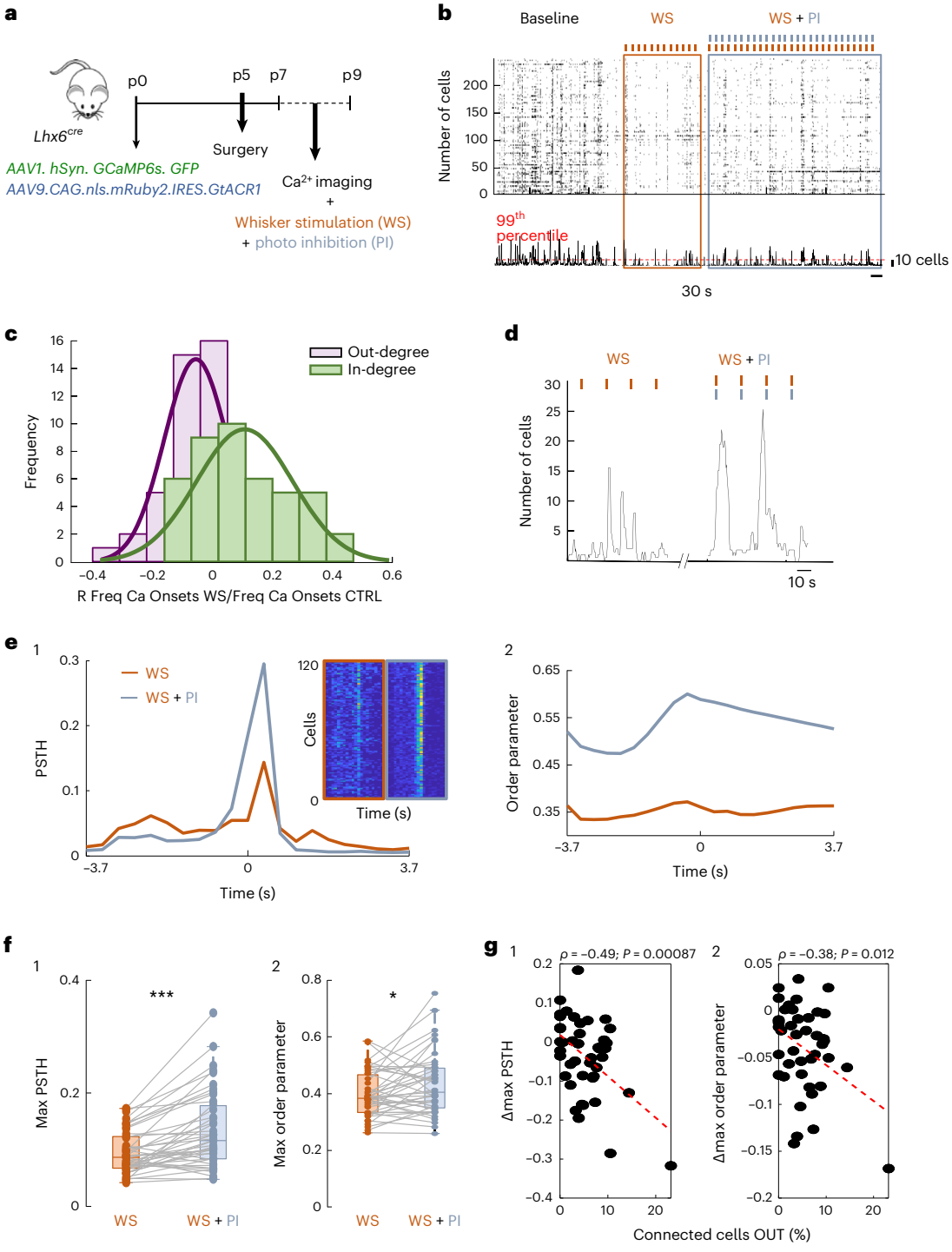

disrupting synchronization, is likely to support the activity-dependent development of cortical circuits. We propose that hub cells contribute to the tailoring of local inhibition to external sensory inputs.

Technical aspects

This study examines the impact of single cells on network dynamics using, to our knowledge for the first time, all-optical approaches at such early postnatal stages. Several studies performed similar experiments in the adult cortex[14,35–41]. The main challenge here was to find the right combination of opsin and calcium indicator that would allow for simultaneous imaging and light activation of immature neurons. Despite their high activity rates, developing cortical cells still display immature firing properties that, in principle, make them less amenable to photoactivation. In addition, the virally induced expression of opsins and GCaMP at early postnatal stages requires early injection methods to allow for sufficient days of virus transfection. Our intracortical injection protocol at birth allows for such stable expression as revealed by a stable number of imaged cells and ratio of imaged GABAergic neurons from p5 to p11. However, it is important to bear in mind that only about half of the GABA neurons identified by their td-Tomato expression co-expressed GCaMP and ST-ChroME, which indicates that some interneurons are excluded from the present analysis. Whether this represents a defined subpopulation of GABA cells remains to be established.

We used GCaMP6s as an indirect reporter of neuronal activity and scanned between 1.5 Hz and 2.7 Hz. Despite this slow sampling rate, we were able to reveal stereotyped chains of neuronal activation occurring within hundreds of milliseconds time windows centered on network bursts, taking advantage of the repetitive sampling of similar events as previously described[5]. In an attempt to find converging methods that would best capture functional connectivity, we compared different approaches: the classical pairwise correlation onset method, excluding zero time lags, using both a binary and a weighted metric as well as generalized transfer entropy[42] (Extended Data Fig. 2). Although these methods produced different values of functional connectivity, we found that all of them predicted a similar order when ranking the cells in increasing order of connectivity degree. With this in mind, we decided to use functional connectivity as measured with pairwise correlation of the binary matrix as it is the representation that better suits for network analysis metrics. Most importantly, the functional connectivity degrees (output and input) measured in this way correlated with the influence of single cells on local circuits as assessed using holographic stimulation. Precise targeting of single neurons expressing the fast soma-targeted opsin ST-ChroME was achieved through an excitation spot matching their soma size (10 µm in diameter). This assures efficient current integration using short illumination time and low excitation power density (0.3–0.5 mW μm^{-2}). The use of a single spot at a time also enabled to achieve a good axial confinement without the need for temporal focusing. Despite the large lateral dimension (10 µm) of the excitation spot, the optical axial confinement of an isolated spot at the power used is expected to be as low as 20 µm, which, combined with the use of a soma-targeted opsin (ST-ChroME), further ensures specificity and cellular resolution by reducing photostimulation of neurites of non-targeted neurons near the target site. Thus, the likelihood of two cells being excited at once is very low, especially when it comes to GABAergic neurons, whose somata are sparse and scattered (on average, 50 µm apart in the developing cortex). The use of a fast opsin also enables, under our imaging conditions, to minimize the excitation crosstalk from the imaging laser for experiments combining functional imaging with optical photostimulation or photoinhibition.

Identities of HC GABA cells and link to in vitro hubs

Our work indicates that HC GABA hub neurons exert greater influence on endogenous and evoked network dynamics than other cells, including HC glutamatergic cells. This is supported by the following observations: (1) cells that reversibly modify network synchrony when activated are mostly GABAergic (31% versus 3% of the glutamatergic cells); (2) the higher an interneuron's input degree, the stronger its influence on spontaneous network synchrony; and (3) the higher an interneuron's output degree, the stronger its influence on sensory-evoked network responses. These HC GABA neurons appear to dampen rather than promote network excitability, because their activation decreases synchronization, and their inhibition promotes it. Of note, we could find cells exerting a significant network influence (that is, reversible) even among poorly connected cells but rarely within glutamatergic cells, in agreement with previous work[5,6,43]. In addition, a single interneuron's impact progressively increased with connectivity rather than appearing specifically restricted to a subpopulation. This linear relationship may reflect the graded developmental stages of the interneuron population resulting from their sequential generation, with the oldest, more developed cells displaying the highest functional degree, as shown in vitro[8] or predicted in silico[44].

However, the present findings bear some differences with previous in vitro work. In particular, operational hub neurons in the developing hippocampus and entorhinal cortex were better defined by their output connectivity degree, indicating that their activation preceded that of other imaged neurons[5,6,43]. In the present study, we found that input hubs were more likely to limit ongoing network dynamics when activated. The difference in the directionality of operational hubs degree, between in vivo and in vitro, may result from the fact that bottom-up inputs conveying sensory information are sectioned in vitro but serve as triggers for network events in vivo. They may also stem from the fact that in vitro work and in vivo work were examining different cortical areas (that is, hippocampal formation versus barrel cortex). This order of neuronal activation initiated by the thalamus is consistent with the observation that input hubs are also the most activated by WS and the most affected by sensory deprivation. Still, the activation of GABA hub neurons most often disrupts network synchronization, both in vitro and in vivo, regardless of the directionality of their functional connectivity (see also below).

Cortical GABAergic interneurons comprise many different subtypes with different developmental journeys and timelines. As discussed above, hub cells appear as the tail of a continuum rather than a discrete subgroup of neurons. Although there is no solid evidence to suggest which cells are more likely to appear in that part of the distribution, it is possible to speculate on who they are. Our experiments performed in $Lhx6^{Cre/+}$ mice suggest that these may comprise either parvalbumin (PV)-expressing or somatostatin (SST)-expressing interneurons, the latter being more likely as SST cells are generated early[8,45], are early transient recipients of thalamic inputs and participate in the proper development of perisomatic GABAergic synapses[32,33].

Circuit mechanisms supporting hub cells activation and their network influence

Because most of the early network bursts are driven in a bottom-up fashion, it is possible that functional input hubs are activated by thalamic inputs, either directly[32] or in a feedback manner, after the activation of local glutamatergic cells. Our imaging lacks the temporal resolution to firmly discriminate between the two possibilities. However, because operational hubs displayed a high input connectivity, it is more likely that their activation is delayed and mediated by their local glutamatergic partners. Accordingly, dual patch-clamp recordings from early born GABA neurons at p5–7 indicate that a significant fraction of these cells form bidirectional synapses with adjacent pyramidal cells[46]. In addition, input hubs are likely connected to other local interneurons, as indicated by the sensory input-dependent rise in functional connectivity within GABAergic cells described here and the presence of transient interconnectivity schemes linking GABA cells[46,47].

This point leads to the discussion of the circuits supporting the impact of operational hub cells. Our experiments indicate that HC

GABA hub cells exert mainly an inhibitory influence on network dynamics. This agrees with previous slice experiments and model predictions[5,48]. It also fits the net excitatory impact of inhibiting functional GABAergic hubs. This suggests that these cells operate mostly through inhibitory GABAergic transmission, in agreement with recent reports indicating an inhibitory network effect of GABA at these postnatal stages in the neocortex in vivo[49,50]. Still, the circuit embedding of functional output GABAergic hubs is not as straightforward. Indeed, these cells are active at the onset of synchronization but do not significantly affect spontaneous network events when activated. Instead, they single-handedly impact evoked network events after WS. One explanation may be that they support feedforward inhibition in response to thalamic inputs, whereas input hubs would support feedback inhibition in response to intracortical inputs. The division of labor between feedforward output and feedback input hubs likely constrains the magnitude of early network events.

Conclusion

We propose that HC GABA neurons support the activity-dependent emergence of a balanced feedforward inhibitory landscape before the onset of active exploration and the opening of the critical period. In addition, GABA hubs may contribute to the regulation of interneuron developmental apoptosis, given their role in neuronal activity coordination. They are, thus, critical players for the proper development of cortical circuits and doorways of susceptibility to developmental disorders.

Online content

Any methods, additional references, Nature Portfolio reporting summaries, source data, extended data, supplementary information, acknowledgements, peer review information; details of author contributions and competing interests; and statements of data and code availability are available at https://doi.org/10.1038/s41593-023-01405-5.

References

1. Martini, F. J., Guillamón-Vivancos, T., Moreno-Juan, V., Valdeolmillos, M. & López-Bendito, G. Spontaneous activity in developing thalamic and cortical sensory networks. *Neuron* **109**, 2519–2534 (2021).
2. Cossart, R. & Garel, S. Step by step: cells with multiple functions in cortical circuit assembly. *Nat. Rev. Neurosci.* **23**, 395–410 (2022).
3. Reh, R. K. et al. Critical period regulation across multiple timescales. *Proc. Natl Acad. Sci. USA* **117**, 23242–23251 (2020).
4. Luhmann, H. J. & Khazipov, R. Neuronal activity patterns in the developing barrel cortex. *Neuroscience* **368**, 256–267 (2017).
5. Bonifazi, P. et al. GABAergic hub neurons orchestrate synchrony in developing hippocampal networks. *Science* **326**, 1419–1424 (2009).
6. Mòdol, L. et al. Spatial embryonic origin delineates GABAergic hub neurons driving network dynamics in the developing entorhinal cortex. *Cereb. Cortex* **27**, 4649–4661 (2017).
7. Feldt, S., Bonifazi, P. & Cossart, R. Dissecting functional connectivity of neuronal microcircuits: experimental and theoretical insights. *Trends Neurosci.* **34**, 225–236 (2011).
8. Picardo, M. A., Guigue, P., Allene, C. & Fishell, G. Pioneer GABA cells comprise a subpopulation of hub neurons in the developing hippocampus. *Neuron* **71**, 695–709 (2011).
9. Khazipov, R. et al. Early motor activity drives spindle bursts in the developing somatosensory cortex. *Nature* **432**, 758–761 (2004).
10. Dooley, J. C., Glanz, R. M., Sokoloff, G. & Blumberg, M. S. Self-generated whisker movements drive state-dependent sensory input to developing barrel cortex. *Curr. Biol.* **30**, 2404–2410 (2020).
11. Dzhala, V., Valeeva, G., Glykys, J., Khazipov, R. & Staley, K. Traumatic alterations in GABA signaling disrupt hippocampal network activity in the developing brain. *J. Neurosci.* **32**, 4017–4031 (2012).
12. Carrillo-Reid, L., Yang, W., Miller, J.-E. K., Peterka, D. S. & Yuste, R. Imaging and optically manipulating neuronal ensembles. *Annu. Rev. Biophys.* **46**, 271–293 (2017).
13. Packer, A. M., Russell, L. E., Dalgleish, H. W. P. & Häusser, M. Simultaneous all-optical manipulation and recording of neural circuit activity with cellular resolution in vivo. *Nat. Methods* **12**, 140–146 (2014).
14. Mardinly, A. R. et al. Precise multimodal optical control of neural ensemble activity. *Nat. Neurosci.* **21**, 881–893 (2018).
15. Ronzitti, E., Emiliani, V. & Papagiakoumou, E. Methods for three-dimensional all-optical manipulation of neural circuits. *Front. Cell. Neurosci.* **12**, 469 (2018).
16. Papagiakoumou, E., Sars, V., de, Oron, D. & Emiliani, V. Patterned two-photon illumination by spatiotemporal shaping of ultrashort pulses. *Opt. Express* **16**, 22039 (2008).
17. Lutz, C. et al. Holographic photolysis of caged neurotransmitters. *Nat. Methods* **5**, 821–827 (2008).
18. Landers, M. & Zeigler, H. P. Development of rodent whisking: trigeminal input and central pattern generation. *Somatosens. Mot. Res.* **23**, 1–10 (2006).
19. Pnevmatikakis, E. A. et al. Simultaneous denoising, deconvolution, and demixing of calcium imaging data. *Neuron* **89**, 285–299 (2016).
20. Rupprecht, P. et al. A database and deep learning toolbox for noise-optimized, generalized spike inference from calcium imaging. *Nat. Neurosci.* **24**, 1324–1337 (2021).
21. Melzer, S. et al. Long-range-projecting GABAergic neurons modulate inhibition in hippocampus and entorhinal cortex. *Science* **335**, 1506–1510 (2012).
22. Madisen, L. et al. A robust and high-throughput Cre reporting and characterization system for the whole mouse brain. *Nat. Neurosci.* **13**, 133–140 (2009).
23. Clauset, A., Shalizi, C. R. & Newman, M. E. J. Power-law distributions in empirical data. *SIAM Rev.* **51**, 661–703 (2009).
24. Honey, C. J., Kötter, R., Breakspear, M. & Sporns, O. Network structure of cerebral cortex shapes functional connectivity on multiple time scales. *Proc. Natl Acad. Sci. USA* **104**, 10240–10245 (2007).
25. Sadovsky, A. J. & MacLean, J. N. Scaling of topologically similar functional modules defines mouse primary auditory and somatosensory microcircuitry. *J. Neurosci.* **33**, 14048–14060 (2013).
26. Yu, S., Huang, D., Singer, W. & Nikolić, D. A small world of neuronal synchrony. *Cereb. Cortex* **18**, 2891–2901 (2008).
27. Broido, A. D. & Clauset, A. Scale-free networks are rare. *Nat. Commun.* **10**, 1017 (2019).
28. Das, A. & Fiete, I. R. Systematic errors in connectivity inferred from activity in strongly recurrent networks. *Nat. Neurosci.* **500**, 1–34 (2020).
29. Mòdol, L. et al. Assemblies of perisomatic GABAergic neurons in the developing barrel cortex. *Neuron* **105**, 93–105 (2019).
30. Golshani, P. et al. Internally mediated developmental desynchronization of neocortical network activity. *J. Neurosci.* **29**, 10890–10899 (2009).
31. Sridharan, S. et al. High-performance microbial opsins for spatially and temporally precise perturbations of large neuronal networks. *Neuron* **110**, 1139–1155 (2022).
32. Tuncdemir, S. N. et al. Early somatostatin interneuron connectivity mediates the maturation of deep layer cortical circuits. *Neuron* **89**, 521–535 (2016).
33. Marques-Smith, A. et al. A transient translaminar GABAergic interneuron circuit connects thalamocortical recipient layers in neonatal somatosensory cortex. *Neuron* **89**, 536–549 (2016).

34. Fogarty, M. et al. Spatial genetic patterning of the embryonic neuroepithelium generates GABAergic interneuron diversity in the adult cortex. *J. Neurosci.* **27**, 10935–10946 (2007).
35. Chettih, S. N. & Harvey, C. D. Single-neuron perturbations reveal feature-specific competition in V1. *Nature* **567**, 334–340 (2019).
36. Carrillo-Reid, L. & Yuste, R. Playing the piano with the cortex: role of neuronal ensembles and pattern completion in perception and behavior. *Curr. Opin. Neurobiol.* **64**, 89–95 (2020).
37. Carrillo-Reid, L., Han, S., Yang, W., Akrouh, A. & Yuste, R. Controlling visually guided behavior by holographic recalling of cortical ensembles. *Cell* **178**, 447–457 (2019).
38. Marshel, J. H. et al. Cortical layer-specific critical dynamics triggering perception. *Science* **365**, eaaw5202 (2019).
39. Rickgauer, J. P., Deisseroth, K. & Tank, D. W. Simultaneous cellular-resolution optical perturbation and imaging of place cell firing fields. *Nat. Neurosci.* **17**, 1816–1824 (2014).
40. Robinson, N. T. M. et al. Targeted activation of hippocampal place cells drives memory-guided spatial behavior. *Cell* **183**, 2041–2042 (2020).
41. Okada, T. et al. Pain induces stable, active microcircuits in the somatosensory cortex that provide a therapeutic target. *Sci. Adv.* **7**, eabd8261 (2021).
42. Wrosch, J. K. et al. Rewiring of neuronal networks during synaptic silencing. *Sci. Rep.* **7**, 11724 (2017).
43. Bocchio, M. et al. Hippocampal hub neurons maintain distinct connectivity throughout their lifetime. *Nat. Commun.* **11**, 4559 (2020).
44. Kaiser, M. Mechanisms of connectome development. *Trends Cogn. Sci.* **21**, 703–717 (2017).
45. Hu, J. S., Vogt, D., Sandberg, M. & Rubenstein, J. L. Cortical interneuron development: a tale of time and space. *Development* **144**, 3867–3878 (2017).
46. Wang, C.-Z. et al. Early-generated interneurons regulate neuronal circuit formation during early postnatal development. *eLife* **8**, 333 (2019).
47. García, N. V. D. M., Karayannis, T. & Fishell, G. Neuronal activity is required for the development of specific cortical interneuron subtypes. *Nature* **472**, 351–355 (2011).
48. Luccioli, S. et al. Modeling driver cells in developing neuronal networks. *PLoS Comput. Biol.* **14**, e1006551 (2018).
49. Kirmse, K. et al. GABA depolarizes immature neurons and inhibits network activity in the neonatal neocortex in vivo. *Nat. Commun.* **6**, 7750 (2015).
50. Murata, Y. & Colonnese, M. T. GABAergic interneurons excite neonatal hippocampus in vivo. *Sci. Adv.* **6**, eaba1430 (2020).

https://doi.org/10.1038/s41593-023-01405-5

Methods

Mice

All animal use protocols were performed under the guidelines of the French National Ethics Committee for Sciences and Health report on 'Ethical Principles for Animal Experimentation' in agreement with European Community Directive 86/609/EEC under agreement APAFIS18125. A total of 82 mice were used in the study (48 females and 34 males). No differences related to the animals' sex were observed. We used double heterozygous *GAD67*$^{Cre/+}$ mice[21] crossed with Ai14 [B6;129S6-Gt(ROSA)$^{26Sortm14(CAG-tdTomato)Hze}$/J] ($n$ = 17) or *RCL-GCaMP6s* (*Ai96*) [B6;129S6-Gt(ROSA)26Sortm96.1(CAG-GCaMP6s)Hze/J] (The Jackson Laboratory) (n = 10) for calcium imaging experiments in vivo (including four pups for the sensory deprivation experiments). *GAD67*$^{Cre/+}$[21] and *Emx1*$^{Cre/+}$ (The Jackson Laboratory) mice were used for imaging combined to holographic stimulation experiments in vivo and 21 (Emx1$^{Cre/+}$ n = 10 and *GAD67*^{Cre} n = 11 pups) and in vitro (n = 7 in total). In addition, eight pups were used for immunohistochemical analysis (Extended Data Fig. 4: *GAD67*$^{Cre/+}$ (n = 5) and *Emx1*$^{Cre/+}$ (n = 3) pups). Seven pups (*Lhx6*$^{Cre/+}$ [B6; CBA-Tg(Lhx6-icre)1Kess/J], The Jackson Laboratory) were used in the photoinhibition experiments (Fig. 4 and Extended Data Fig. 10). All crossings were performed at 7–8 weeks of age. All efforts were made to minimize both the suffering and the number of animals used. No developmental abnormalities or aberrant activity was observed in *GAD67*$^{Cre/+}$; *Ai96*[63].

Virus injections

To perform large-scale calcium imaging, pups were injected at birth with a viral solution (titer, 10^{12} genome copies per milliliter; Penn Vector Core) of *AAV1.hsyn.GCaMP6s.WPRE.SV40* (Penn Viral Core). Additionally, to perform the photostimulation and the photoinhibition experiments, *AAV9.CAG.DIO.ChroME-ST.mRuby3* or *AAV9.CAG.nls.mRuby2.IRES.GtACR1* (both a generous gift from Hillel Adesnik, University of California, Berkeley) were injected at p0. Virus stock was diluted 1:2 for the *AAV1.syn.GCaMP6s.WPRE.SV40* or 1:4 for the *AAV9.CAG.DIO.ChroME-ST.mRuby3* and *AAV9.CAG.nls.mRuby2.IRES.GtACR1*. Mice were separated from the dam and anesthetized by hypothermia. The procedure lasted approximately 10 min to minimize separation from the dam. Glass micropipettes with a tip of 30–45-µm diameter attached to a Nanoject (Drummond Scientific) injector were used for injections. A total amount of 300 nl of virus was injected in the cortex 200 µm below the surface (RC: 0.5 mm; ML: 1.85 mm) or intraventricularly. Location of injection sites was confirmed postmortem and after the imaging (Extended Data Figs. 1 and 4). Pups were allowed to recover on a heating pad at 37 °C and then returned to the dam. We did not observe any neglecting or consuming behavior after this procedure.

Cranial window surgery

All procedures were performed following ref. 51. In brief, betadine and lidocaine (cream) were applied to the skin adjacent to the intended incision 20 min before starting the surgical procedures. Mice aged between p4 and p11 (both male and female) were anaesthetized with isoflurane (1.5% via a nose cone) and placed in a stereotaxic frame containing a heating pad with bedding. All surgical instruments were sterilized. After skin removal, a custom-made head plate containing two 3.5-mm-diameter holes was fixed to the skull using the veterinary adhesive Vetbond (3M Vetbond Tissue Adhesive). Once the head plate was fixed and stabilized and the pup was comfortably placed in a warm cotton bed, a ~3-mm-diameter craniotomy was performed over the primary somatosensory barrel cortex and covered with a glass coverslip. Care was taken not to damage the dura or the underlying vessels during the procedure. A glass window was then sealed with uncured Kwik-Sil (WPI) and fixed to the head plate using Vetbond to re-ensure the stability of the window. The head plate was then fixed to the skull using Super Bond (DSM Dentaire). Body temperature was continuously monitored and maintained at close to physiological values (34–37 °C) by means of a heating pad during the whole surgical process.

In vivo two-photon imaging

After the surgical procedure, pups were allowed to recover for 90 min in the same stereotaxic frame where the craniotomy was done. It contained cotton bedding and a heating pad. Throughout this period and the following experiments, pups were constantly monitored and fed with veterinary milk ad libitum. They typically remained calm while head-fixed, allowing calcium imaging experiments that lasted 2–3 h. Mice did not exhibit any sign of pain or distress during the in vivo imaging. Movies were 1,800 or 3,600 frames at 512 × 512 pixels. Each movie lasted approximately 20 min. Imaging was performed with a two-photon microscope (TriM Scope II, LaVision BioTec). The Ti:sapphire excitation laser (Chameleon Ultra II, Coherent) was operated at 920 nm with a maximum 35-mW power under the objective lens. GCaMP fluorescence was isolated using a bandpass filter (510/25). Images were acquired through a GaAsP photomultiplier tube (H7422-40, Hamamatsu) using a ×16 immersion objective (Nikon, NA 0.8). Using Imspector software (LaVision BioTec), the fluorescence signal from a 600 × 600-µm^2 FOV was acquired at 1.5 Hz or 2.7 Hz with, respectively, 2.54-µs or 1.2-µs dwell time per pixel (1.17 µm per pixel). Movies at a faster frame rate (5 Hz, 7 Hz and 8 Hz) were also acquired to probe our temporal resolution. Because spontaneous activity during development is typically on the low range kinetics, we found that dynamics were similar in low and high scanning rates. Movies from non-overlapping FOVs were performed in the same pup and used for the analysis (FOVs are indicated in their respective figure legends as imaging sessions).

Two-photon imaging and holographic stimulation in vivo

The optical system was a custom-built microscope combining galvo-based two-photon scanning with computer-generated holography[52–54]. Raster scanning of calcium fluorescence signals was achieved using standard galvo scanners and a pulsed femtosecond imaging laser source. The laser beam (Chameleon Ultra II, Coherent) was expanded with two-lense telescope assembly (f = 300 mm, f = 500 mm) and projected onto an x–y galvo mirror pair (6215H, Cambridge Technology) controlled with two servo driver cards (67125H-1HP-FS60, Cambridge Technology). A half-wave plate (AWHP10M-980, Thorlabs) and a polarizer (GT10-B, Thorlabs) were used to adjust laser power. Next, a scan and a tube lens (focal length f_S = 50 mm and f_T = 375 mm, respectively) were used to conjugate the x–y scanner focal plane to the back focal plane of the microscope objective (×16 Nikon, NA 0.8). This configuration allowed scanning an FOV of 350 × 350 µm (512 × 512 pixels) at the focal plane of the objective with a framerate of 2.7 Hz and a power of 25 mW at 920-nm wavelength. To collect the emitted fluorescent signal, the back focal plane of the objective and the focal plane of a GaAsP photomultiplier tube (Hamamatsu, H7244-20) were conjugated through a relay of lenses (f = 100 mm, AC254-100-A, Thorlabs, f = 25 mm, LA1951-A, Thorlabs). Two spectral filters were mounted in front of the photomultiplier tube (FF01-770/SP-25, Semrock, ET520/40m, Chroma) to optimize GFP detection. The analog signal was next converted from current to voltage and amplified through a transimpedance amplifier (TIA60, Thorlabs). Finally, an electronic card (NI6356, National instruments) in combination with ScanImage software (Vidrio Technologies) was used to control the scanners and to digitalize the analog signal from the photomultiplier tube.

Photostimulation of neurons of interest used computer-generated holography. In brief, the beam of the pulsed femtosecond photoactivation laser (Goji, Amplitude Systems, 10-MHz repetition rate, 1,030 nm) was shaped by a spatial light modulator (SLM) (Hamamatsu, LCOS-SLM X13138-07). The size of the laser beam was expanded using a two-lense telescope assembly (AC254-030-B, Thorlabs, AC254-150-B, Thorlabs) so that it covered the entire surface of the SLM. A half-wave plate

(AHWP10M-980, Thorlabs) was used to align the polarization of the laser to the orientation of the liquid crystals. Three lenses (AC508-300-B) combined with the tube lens (f_T = 375 mm) in 4-f configuration enabled conjugating the SLM focal plane to the back focal plane of the microscope objective. The zero-order of the SLM was suppressed with a cylindrical lens (f = 300 mm, f = LJ1558L1-B, Thorlabs) as described previously[55]. A custom software (Wavefront Designer IV) based on the Gerchberg–Saxton algorithm was used to convert the photostimulation intensity pattern at the focal plane into a photostimulation phase mask addressed to the SLM[17].

To combine the two imaging and photostimulation paths, a dichroic mirror (DMPSP1000L, Thorlabs) was placed at the focal plane of the scan lens. The custom software mentioned above was used to adjust the spatial overlap of the photostimulation pattern with the imaging at 920 nm owing to a rhodamine fluorescent sample that was bleached at 1,030 nm and imaged at 920 nm. To synchronize the paths, a MATLAB script defined a photostimulation temporal gate and sent a TTL signal via the NI card described above to an obturator (Vincent Sutter Instrument) placed in front of the photostimulation laser source during the raster scanning for calcium imaging. Holographic stimulation of targeted cells was achieved with an excitation spot of 10-µm lateral size, corresponding to an axial resolution of 20 µm. Trains of 10 consecutive pulses (10-ms duration, at 10 Hz or 40 Hz, at 0.3–0.8 mW µm^{-2} power) were applied every 10 s during the stimulation period.

In vitro patch-clamp recordings and optogenetics

Coronal slices (300 µm thick) were obtained from *GAD67*$^{Cre/+}$, *Emx1*$^{Cre/+}$ (Extended Data Fig. 5) or *Lhx6*$^{Cre/+}$ (Extended Data Fig. 8) between p7 and p10 in pups injected at birth with AAV9.CAG.DIO.ChroME-ST.mRuby3 (Extended Data Fig. 5) or with AAV9.CAG.nls.mRuby2.IRES.GtACR1casac (Extended Data Fig. 9), using a Leica VT1200 S vibratome in ice-cold oxygenated modified artificial cerebrospinal fluid (ACSF) (in nM): 2.5 KCl, 1.25 NaH_2PO_4, 7 $MgCl_2$, 5 $CaCl_2$, 26 $NaHCO_3$, 5 D-glucose and 126 CholineCl. Slices were then kept for rest (1 h, room temperature) in oxygenated normal ACSF containing (in mM): 126 NaCl, 3.5 KCl, 1.2 NaH_2PO_4, 26 $NaHCO_3$, 1.3 $MgCl_2$, 2.0 $CaCl_2$ and 10 D-glucose. Patch-clamp recordings were carried out using a SliceScope Pro 1000 Rig (Scientifica) equipped with a CCD camera (Hamamatsu, Orca-05G). Slices were transferred to a submerged recording chamber and continuously perfused with oxygenated ACSF (3 ml min^{-1}) at ~32 °C. Electrodes (4–8-MΩ resistance) were pulled using a PC-10 puller (Narishige) from borosilicate glass capillaries (GC150F-10, Harvard Apparatus) and filled with a filtered current-clamp intracellular solution containing (in mM): 125 K-methylSO_4, 15 KCl, 5 NaCl, 10 HEPES, 2.5 Mg-ATP, 0.3 Na-GTP (pH 7.3 and ~280 mOsm). Electrophysiological signals were amplified (Multiclamp 700B), low-pass filtered at 2.9 kHz, digitized at 10 kHz and acquired using a Digidata 1440A digitizer and pClamp 10 software (all from Molecular Devices). An optoLED system (Cairn Research) consisting of two 3.5-W LEDs was used. A 470-nm LED coupled to a GFP filter cube was used to activate ChroME-expressing or GtACR1-expressing neurons (ChroME: 10-ms per pulses; GtACR1: 10 ms or 1 s per pulses). A white LED coupled to an RFP filter cube was used to visualize ChroME/mRuby-expressing or GtACR1/mRuby-expressing neurons. Light was delivered using a ×40 objective, leading to an illumination field of ~1 mm^2. For ChroMe-expressing neuron stimulation, spikes were evoked by trains of 10 pulses (10 ms at 10 Hz or 40 Hz) at different intensity power (0.1, 0.2 and 0.5 mW mm^{-2}). The response delay, the number of spikes and their amplitude were measured with Clampfit 10.7 (Molecular Devices). For GtACR1-expressing neuron stimulation, the photocurrent evoked by a 1-s or 10-ms light pulse was measured. Two protocols were used to observe the effect of GtACR1 stimulation when neurons fired: (1) a 1-s continuous light pulse at different intensity powers (0.1, 0.2 and 0.5 mW mm^{-2}) applied simultaneously with a 4-s suprathreshold depolarizing step; and (2) a train of 10 light pulses (10-ms at 10 Hz) at different intensity powers (0.1, 0.2 and 0.5 mW mm^{-2}) applied simultaneously with a 1-s suprathreshold depolarizing step. The number of spikes during the depolarizing step and the delay between the last spike before the light pulses and the following spike were measured with Clampfit 10.7.

WS

Air puffs (100-ms duration every 4 s) were delivered (Picospritzer III, Parker Hannifin) via a 1-mm-diameter plastic tube placed perpendicularly to the contralateral whiskers (at about 20 mm distance). Stimulation was directed to the snout. Pressure was adjusted to avoid a startle response.

Sensory deprivation

At p1–2, mice were briefly removed from the dam and anesthetized by hypothermia (10 min); all whiskers were plucked using sterile forceps. Pups were allowed to recover on a heating pad before returning to their dam.

Analysis of calcium dynamics

Cell and calcium transients detection. To remove possible confounding due to light artifacts, we removed frames where the stimulation occurred and interpolated the values using the previous and consecutive frame before motion correction and deconvolution. Movies were first motion corrected using a rigid registration method (NormCorre)[56]. The FOV was split into overlapping patches of 1/4th and then 1/8th of the spatial dimension. During registration, a rigid translation was estimated for each frame for each patch by matching it to a template (initially the median image of the first 250 frames). Each registered frame was then used to update the running mean of previously registered frames. For each of the conditions, two iterations were run, decreasing the maximum shift allowed for each patch. Next, using the same patch dividing scheme and method as above, an FFT-based algorithm was used[57], which upsampled the signal after the initial registration and allowed for a smooth motion field that was applied to account for non-rigid movement between patches.

Contours and calcium transients were detected using the constrained non-negative matrix factorization framework (CaImAn)[19]. Calcium traces were extracted using the 20th percentile and using a window of 200 frames to de-trend the data. When imaging at 1.5 Hz, the data were rescaled between 0 and 5 and then deconvolved using CASCADE[20], whereas no rescaling was used for recordings at 2.7 Hz. We then binarized the spiking probability, where a probability of larger than 0.8 was used to indicate spiking activity for a given frame.

Calcium onset detection. Calcium onsets were obtained as a coarse-grained representation of neuronal activity. A calcium onset was detected using the normalized calcium trace of each cell, guaranteeing that the calcium signal was contained within [0, 1] and then smoothed using a filter based on a Gaussian kernel (C_{norm}). We then calculated $\Delta C_{norm}/\Delta t$ and detected positive peaks in the derivative separated by at least four frames using a minimum peak threshold of $\mu(C_{norm}) + ¼\,\sigma(C_{norm})$.

Functional connectivity. The relative delays of cell activation onsets were used to define the functional connectivity of the network (three frames when imaging at 1.5 Hz and four frames when imaging at 2.7 Hz). For each pair of cells, two statistical tests were made on the distribution of their onset time difference to assess whether or not they were connected—first, a uniformity test (Kolmogorov–Smirnov, with a threshold at 5% significance level) to discard homogeneous distributions and, second, a *t*-test (with a threshold at 0.01) to discard distributions centered at 0. If the results of the two tests were significant, the two cells were functionally linked, and the sign of the mean delay was used to define the direction of the link.

Network measures. All measures that we implemented used algorithms from the Brain Connectivity Toolbox (www.brain-connectivity-toolbox.net)[58].

Network topology

To determine the overall topology, we followed a strategy described in ref. 23 implemented using the powRlaw package[59]. We tested the continuous distribution of connectivity degrees in three steps after removing cells with zero connections for which the logarithm is not defined:

1) Estimation of the parameters of a power law given the data using a continuous distribution.
2) Generation of power law surrogate distributions with the parameters established in 1. We then compare the fit of the empirical data with the surrogate distributions using a log-likelihood test.

3a If the fits are indistinguishable, the power law fit is compared with a log-normal and an exponential distribution using Vuong's closeness test.
3b If there is a significant difference between the empirical data and the surrogate distributions, we reject the hypothesis that the underlying distribution is a power law, and we, instead, compare a log-normal and exponential distribution. We then choose the better fit using Vuong's closeness test.

Network density

Density is the ratio between the number of observed connections and the number of all possible connections. For a directed graph, it is defined as follows:

$$\frac{C}{N^2}$$

where C is the number of observed connections, and N is the total number of nodes.

Connected component

Two nodes belong to the same connected component if there is a path connecting them. We then found the largest set of nodes that are mutually reachable according to these criteria. Finally, we express the proportion of nodes belonging to this subgraph as a proportion of all cells.

Network synchronization. As a time-dependent synchronization measure of network activity, we computed the Kuramoto order parameter[60]. Starting from the binary representation obtained from calcium onsets, we first computed the firing phase of each cell $\boldsymbol{\varphi}_i(t)$ using a linear interpolation between the points $(t_k, -\pi)$ and (t_{k+1}, π), where t_k represents the times of calcium onsets. Once the phase was computed for all cells, the Kuramoto order parameter can be defined as

$$KOP(t) = \frac{1}{N}\left|\sum_{i}^{N} \exp(j\varphi_i(t))\right|$$

where j is the imaginary unit. The Kuramoto order parameter takes values in the interval [0, 1], where 1 indicates perfect synchrony and 0 represents completely asynchronous dynamics. Intermediate values quantify the varying level of network synchronization.

Hub cell test. To assess whether the stimulation of a cell had an impact on network dynamics, we used the Kuramoto order parameter. A cell was defined as significantly modulating network dynamics when the following three conditions on the median values of the order parameter across epochs were met: (1) significantly different between stimulation period and baseline; (2) significantly different from stimulation period and post-stimulation; and (3) not significantly different between baseline and post-stimulation. All tests were performed using a Wilcoxon rank-sum test ($P < 0.0001$).

Whisker modulation. To determine the effect of photoinhibition of single GABA cells during whisker stimulation, we computed the average PSTH of the calcium onsets across cells centered on the time of WS (±10 frames). This was done during regular WS ($PSTH_{WS}$) and during WS with photoinhibition ($PSTH_{WS+PI}$). We also computed the average Kuramoto order parameter centered at WS in both scenarios (KOP_{WS} and KOP_{WS+PI}) within the same ±10 frames. To quantify the effect that photoinhibition produced on the two metrics, we extracted the maximum of these two quantities both during WS and WS + PI. With this, we calculated the difference between the maxima as $\Delta\max(PSTH) = \max(PSTH_{WS}) - \max(PSTH_{WS+PI})$ and $\Delta\max(KOP) = \max(KOP_{WS}) - \max(KOP_{WS+PI})$. Using the out-degree of the photo-inhibited cell, we computed the correlation coefficient between the difference of maxima described above and the degree of the cell. We also analyzed the relationship between whisker modulation and neuron's degree as follows. For each one of the $n = 37$ FOVs, we computed the correlation coefficients of the in-degree and out-degree of the cell and the relative change in the frequency of calcium onsets during WS with respect to control ($\mathbf{v}_{CaOnset\text{-}WS}/\mathbf{v}_{CaOnset\text{-}CTRL}$).

Histology

Pups were were deeply anaesthetized with a mix of Domitor and Zoletil (0.6 mg kg^{-1} and 40 mg kg^{-1}, respectively, *GAD67*^{Cre};*Ai14* ($n = 8$), *GAD67*^{Cre} ($n = 8$) and *Emx1*^{Cre} ($n = 3$)) and transcardially perfused with saline, followed by 4% paraformaldehyde (PFA) before brain extraction at p5 ($n = 3$), p8 ($n = 14$) or p11 ($n = 2$). Brains were post-fixed overnight at 4 °C and washed in PBS, and 70-µm-thick coronal sections were obtained using a vibratome (Leica). Coronal brain sections from fixed brains (70-µm-thick sections) were then processed to quantify the GCaMP6s expression among GABAergic population (Extended Data Fig. 1) or the co-expression of ST-ChroME and GCaMP6s expression in the *Emx1*^{Cre} or the *GAD67*^{Cre} pups at p8 (Extended Data Fig. 4). No additional labeling was performed on the brain slices. Quantification was performed after mounting the sections with a mounting medium (VECTASHIELD, Antifade Mounting Medium, Vector Labs).

Statistics and reproducibility

Data are given as mean ± s.e.m. or median and interquartile range. Sample sizes were chosen based on a previous study[29] and took into consideration the three Rs principle. Data collection and analysis were not performed blinded to the conditions of the experiments. Instead, experiments were performed by two groups of independent researchers, converging toward the same results. Randomization in this study was performed using animals from different sex and litters. Additionally, in vivo experiments were performed at different day times. None of the mentioned randomization measures had an impact on the results obtained. Statistics and graphs were performed using Prism 7 and 9 (GraphPad Software), MATLAB (MathWorks) or R (R Foundation for Statistical Computing). All values obtained were included unless stated otherwise in the relevant Methods subsections. The respective statistical tests that were used are indicated in the figure legends. A *t*-test and one-way or two-way ANOVA were used in samples following a normal distribution. To correct for multiple comparisons, we performed Bonferroni's or Tukey's post hoc test when necessary. Non-parametric statistical analysis using Mann–Whitney, Wilcoxon (paired samples), Kruskal–Wallis or Kolmogorov–Smirnov tests were performed for datasets not following a normal distribution. Dunn's post hoc test was applied when necessary. We have made the data used in this study available.

Reporting summary
Further information on research design is available in the Nature Portfolio Reporting Summary linked to this article.

Data availability
All data supporting the findings of this study are available from https://gitlab.com/cossartlab/. Source data are provided with this paper.

Code availability
All the codes used to extract and analyze the data illustrated in the figures are freely accessible at https://gitlab.com/cossartlab/.

References

51. Golshani, P. & Portera-Cailliau, C. In vivo 2-photon calcium imaging in layer 2/3 of mice. *J. Vis. Exp.* 681 (2008).
52. Chaigneau, E. et al. Two-photon holographic stimulation of ReaChR. *Front. Cell. Neurosci.* **10**, 234 (2016).
53. Ronzitti, E. et al. Submillisecond optogenetic control of neuronal firing with two-photon holographic photoactivation of Chronos. *J. Neurosci.* **37**, 10679–10689 (2017).
54. Chen, I.-W. et al. In vivo sub-millisecond two-photon optogenetics with temporally focused patterned light. *J. Neurosci.* **39**, 3484–3497 (2019).
55. Hernandez, O., Guillon, M., Papagiakoumou, E. & Emiliani, V. Zero-order suppression for two-photon holographic excitation. *Opt. Lett.* **39**, 5953–5956 (2014).
56. Pnevmatikakis, E. A. & Giovannucci, A. NoRMCorre: an online algorithm for piecewise rigid motion correction of calcium imaging data. *J. Neurosci. Methods* **291**, 83–94 (2017).
57. Guizar-Sicairos, M., Thurman, S. T. & Fienup, J. R. Efficient subpixel image registration algorithms. *Opt. Lett.* **33**, 156–158 (2008).
58. Rubinov, M. & Sporns, O. Complex network measures of brain connectivity: uses and interpretations. *Neuroimage* **52**, 1059–1069 (2010).
59. Gillespie, C. S. Fitting heavy tailed distributions: the poweRlaw package. *J. Stat. Softw.* **64**, 1–16 (2015).
60. Rodrigues, F. A., Peron, T. K. D., Ji, P. & Kurths, J. The Kuramoto model in complex networks. *Phys. Rep.* **610**, 1–98 (2016).

Acknowledgements
We thank C. Dussaux and A. Barrat for helpful discussions on previous versions of the manuscript and constructive feedback. We thank L. Cagnacci, C. Pauchet-Lopez, F. Michel (InMAGIC imaging facility) and INMED's animal facility technicians for excellent technical support. We are grateful to V. Crépel and A. Represa for sharing equipment. We thank E. Papagiakoumou for the helpful discussion on the design of the microscope setup. We also thank all Cossart laboratory members for useful comments on this manuscript. This work was supported by the European Research Council under the European Union's Horizon 2020 research and innovation program (grant agreement nos. 646925 and 951330), by the Fondation Bettencourt Schueller, by the Fondation Roger de Spoelberch and by the French National Research Agency (grant agreement no. ANR-14-CE13-0016). A.B. and R.C. are supported by CNRS. E.L. is supported by the Ministère de l'Enseignement Superieur et de la Recherche. E.R. received funding from the European Research Council Synergy Grant scheme (Helmholtz, ERC grant agreement no. 610110). V.E. acknowledges the Fondation Bettencourt Schueller (Prix Coups d'Elan pour la Recherche Française) and the ERC Advanced Grant HOLOVIS (ERC-2019-AdG, award no. 885090).

Author contributions
L.M., Y.B., T.T. and R.C. designed the research. L.M., Y.B., T.T., E.L., S.B., A.B., A.V., R.D., M.A.P. and J.-C.P. performed experiments. L.M., Y.B. and D.A. analyzed data. L.M., Y.B., D.A. and R.C. wrote the paper. E.R. designed the optical system for holographic stimulations, with V.E., T.T., R.S., I.B. and S.B. V.D. conceived and developed the Wavefront Designer IV software, with V.E. H.A. provided the opsin viruses. R.C. conceived and supervised the project.

Competing interests
The authors declare no competing financial interests.

Additional information
Extended data is available for this paper at https://doi.org/10.1038/s41593-023-01405-5.

Supplementary information The online version contains supplementary material available at https://doi.org/10.1038/s41593-023-01405-5.

Correspondence and requests for materials should be addressed to Rosa Cossart.

Peer review information *Nature Neuroscience* thanks the anonymous reviewers for their contribution to the peer review of this work.

https://doi.org/10.1038/s41593-023-01405-5

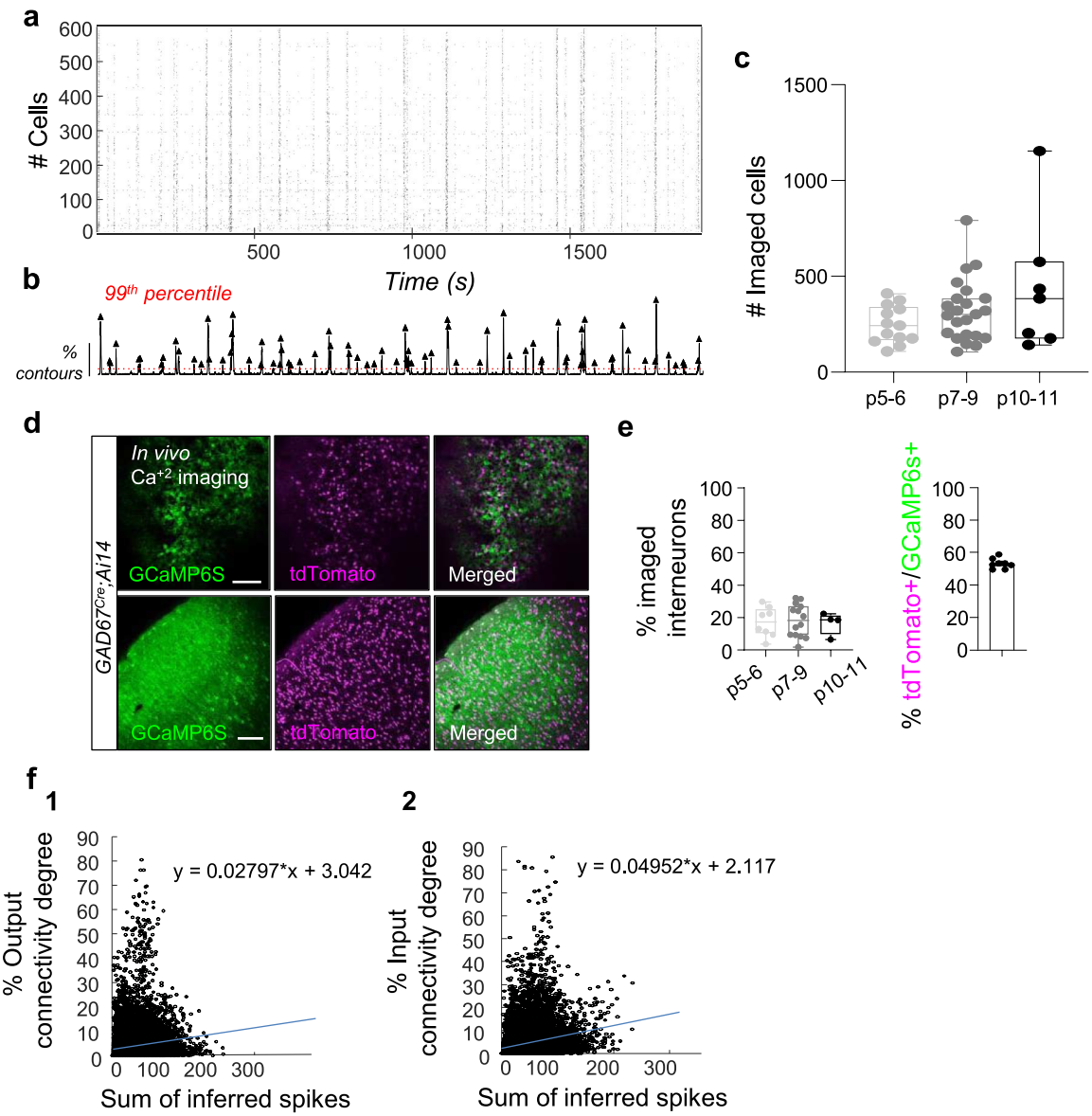

Extended Data Fig. 1 | a, Representative rasterplot of the onsets of calcium events onsets occurring in imaged neurons within an imaging session at p8; all cells are labeled using viral expression of GCaMP6s (AAV1-Syn-GCaMP6s); (b) the corresponding sum of active contours as a function of time is plotted in the histogram below; red dotted line indicates the number of coactive neurons above which synchronous activity exceeds chance level (99th percentile) and black triangles indicate detected Spontaneous Calcium Events. c, Box plot indicating number of imaged cells at different developmental stages. One-way ANOVA: F(2,40) = 2.29; p = n.s. n = 12 FOVs p5-6 (3 females and 2 males); n = 23 FOVs p7-9 (4 females and 5 males); n = 8 FOVs p10-11 (4 females and 3 males). Each dot represents a FOV. **d**, Upper panels, z projection of in vivo GCaMP6s and tdTomato (Ai14 + GABAergic cells) expression. Scale bar 100 µm. Lower panels show viral expression at p8 of AAV1GCaMP6s in a coronal section (70 µm) of a pup injected at p0. **e** Left panel: Box and whiskers indicates the fraction of GABA neurons (expressing tdTomato) among the active cell population as a function of age. No differences were observed between ages: p5-6 = 18 ± 2.7 (n = 8 FOVs); p7-9 = 17 ± 3.2 (n = 14 FOVs); p10-11 = 17 ± 3.5 (n = 4 FOVs). Each dot represent a FOV. Right panel: Bar plot show the percentage of interneurons expressing GCaMP6s (n = 8 pups, 5 females and 3 males). Each dot represents a pup. **f**, Distribution of the median % output (1) and input (2) connectivity degree as a function of inferred spikes. Correlation with the % of Output connectivity degree: y = 0.02797*x + 3.042; Correlation with the % of Input connectivity degree: y = 0.04952*x + 2.117. Data in panel c and e (left panel) is presented as Median and Interquartile range. Data in panel e (right panel) is given as mean ± SEM.

https://doi.org/10.1038/s41593-023-01405-5

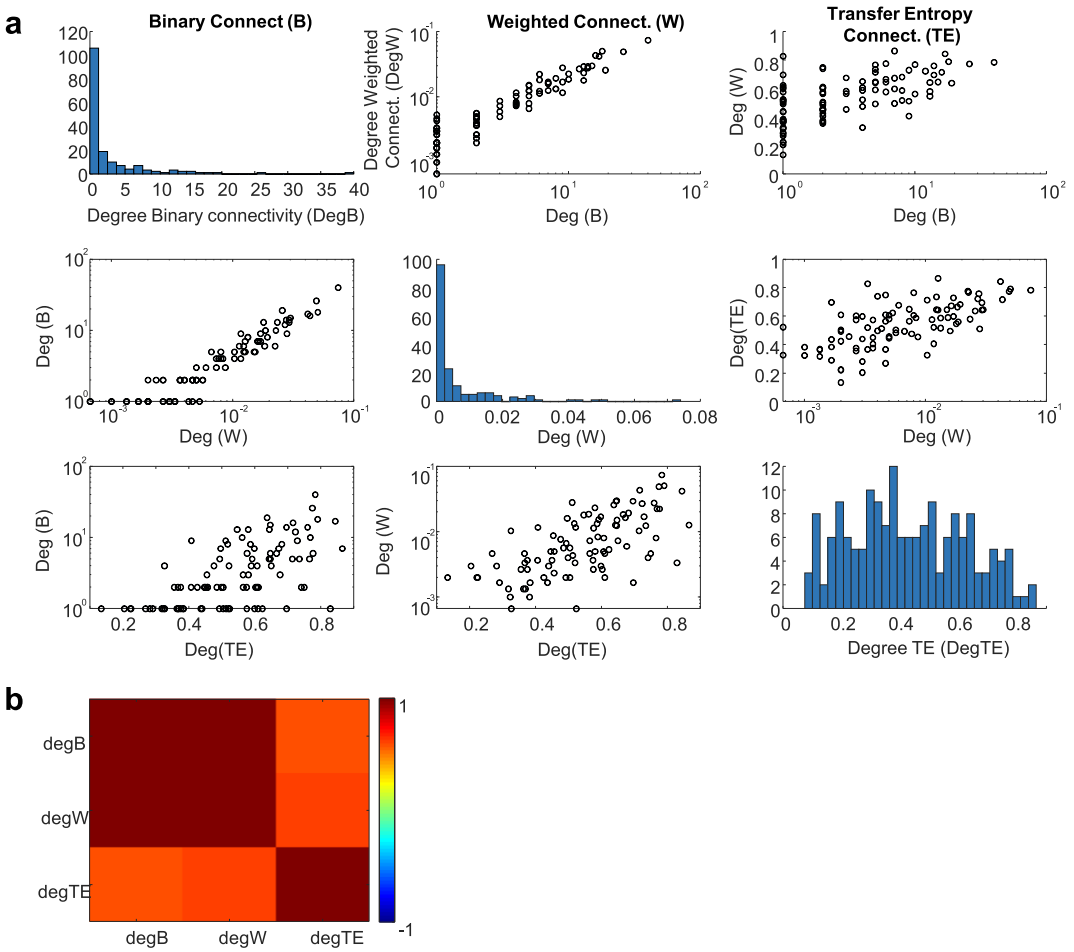

Extended Data Fig. 2 | a, Comparison of three different methods for calculating functional connectivity. In the diagonal: Distribution of out-degree obtained via Functional Connectivity calculated using 1) binary representation of the connectivity matrix as in main text. 2) weighted connectivity matrix, i.e, same as 1) but the value (i,j) of the connectivity matrix is the strength of the connection extracted as the maximum value of normalized crosscorrelation within the +/−4 frames between spike train i and j. 3) Connectivity matrix with the entry (i,j) as the Maximum value of transfer entropy between spike train i and j in the same +/−4 frames. While we only expect to obtain heavy tail distributions when quantifying the degree of the binary connectivity matrix -only measure that uses whole numbers-, the degrees calculated with all methods follow a similar degree rank, as seen by the positively correlated scatter plots of the degree values using the three methods (off- diagonal plots). **b**, Heatmap representing the average correlation between the degrees calculated using the three methods described above across the n = 23 FOVs which corresponds to p7 up to p9.

https://doi.org/10.1038/s41593-023-01405-5

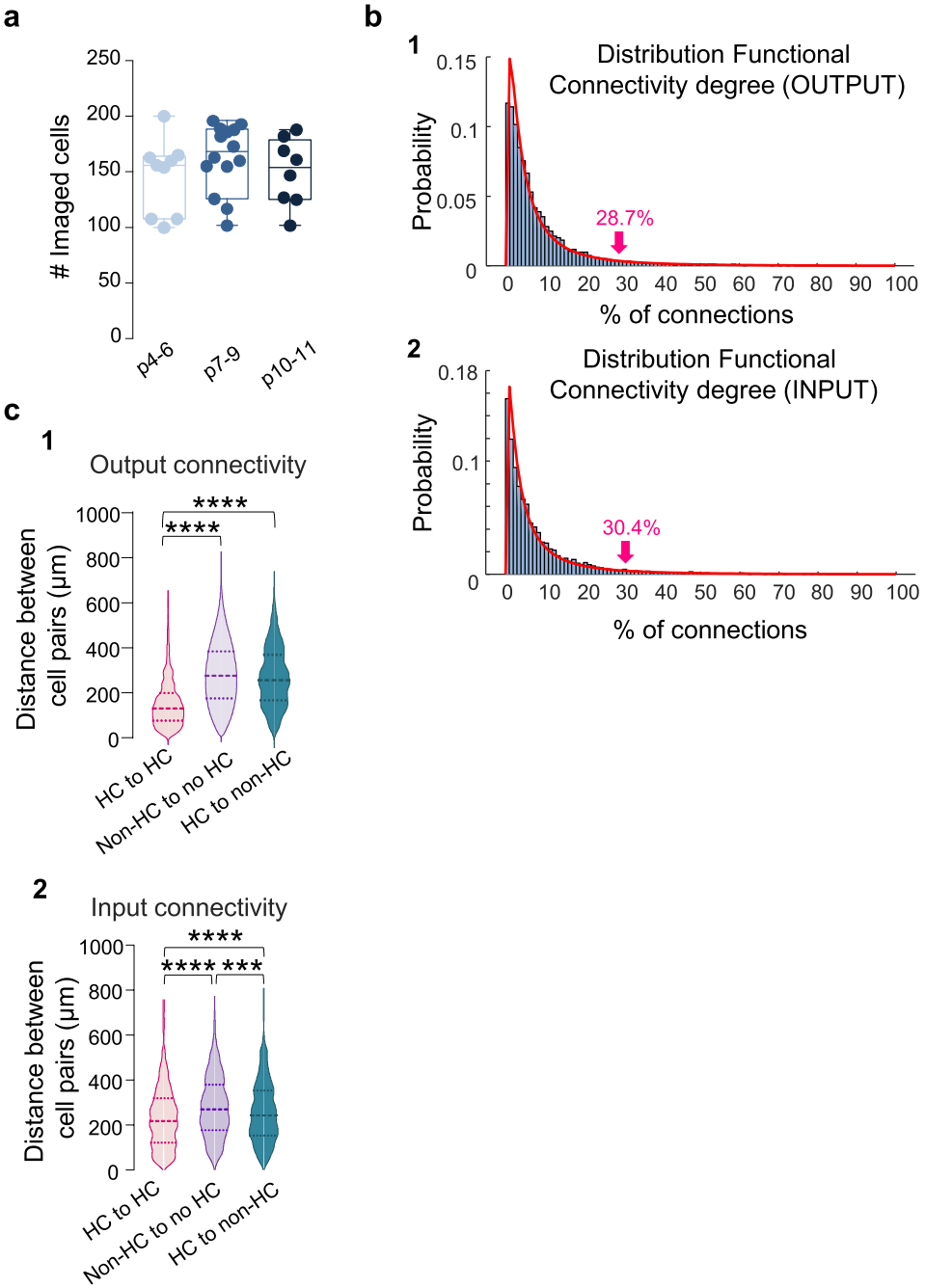

Extended Data Fig. 3 | a, Box plots indicate number of recorder GCaMP6s positive cells as a function of age. One-way ANOVA: $F(2,25) = 0.68$; $p = .n.s.$ n = 9 FOVs at p4-6 (3 females and 1 male); n = 12 FOVs at p7-9 (1 female and 2 males); n = 8 FOVs at p10-11 (2 females and 1). Each dot represents a FOV. Data are given as median and interquartile range. **b**, Distribution of the functional output (1) and input (2) connectivity (fraction of active) of all imaged GABA neurons (n = 4740) in the three age groups. The data is best fitted using a log normal distribution (see methods). Arrows and numbers in pink indicate the connectivity of HC cells (95th percentile) for OUTPUT (28.7%) and INPUT (30.4%). **c**, Violin plots showing differences in the anatomical distance between HCout_global(1) and HCin_global (2) GABAergic cells (pink), as well as HC cells and non-HC cells (purple) and bet non-HC cells (blue). (1) Output connectivity: One-way ANOVA: $F(2, 2997) = 298.0$; $p < 0.0001$. Tukey's (two-sided) post hoc comparison indicates differences between the distance of HC to HC vs. Non- HC to no HC ($p = 1.45e\text{-}90$) and HC to HC vs HC to non-HC ($p = 1.05e\text{-}97$). (2) Input connectivity: One-way ANOVA: $F(2, 2997) = 35.47$; $p < 0.0001$. Tukey's (two-sided) post hoc comparison indicates differences between the anatomical distance between HC cells vs HC and non-HC cells ($p = 1361e\text{-}09$), HC cells vs HC to non-HC cells ($p = 396e\text{-}18$), and between the distance of Non-HC (among themselves) and the distance of HC to Non-HC cells ($p = 0.01$). Data is panels a and c is presented as Median and interquartile range. Box and whiskers statistics correspond to the analysis performed with the mean value of each animal across all recorded FOVs. Each data point represent a FOV.

https://doi.org/10.1038/s41593-023-01405-5

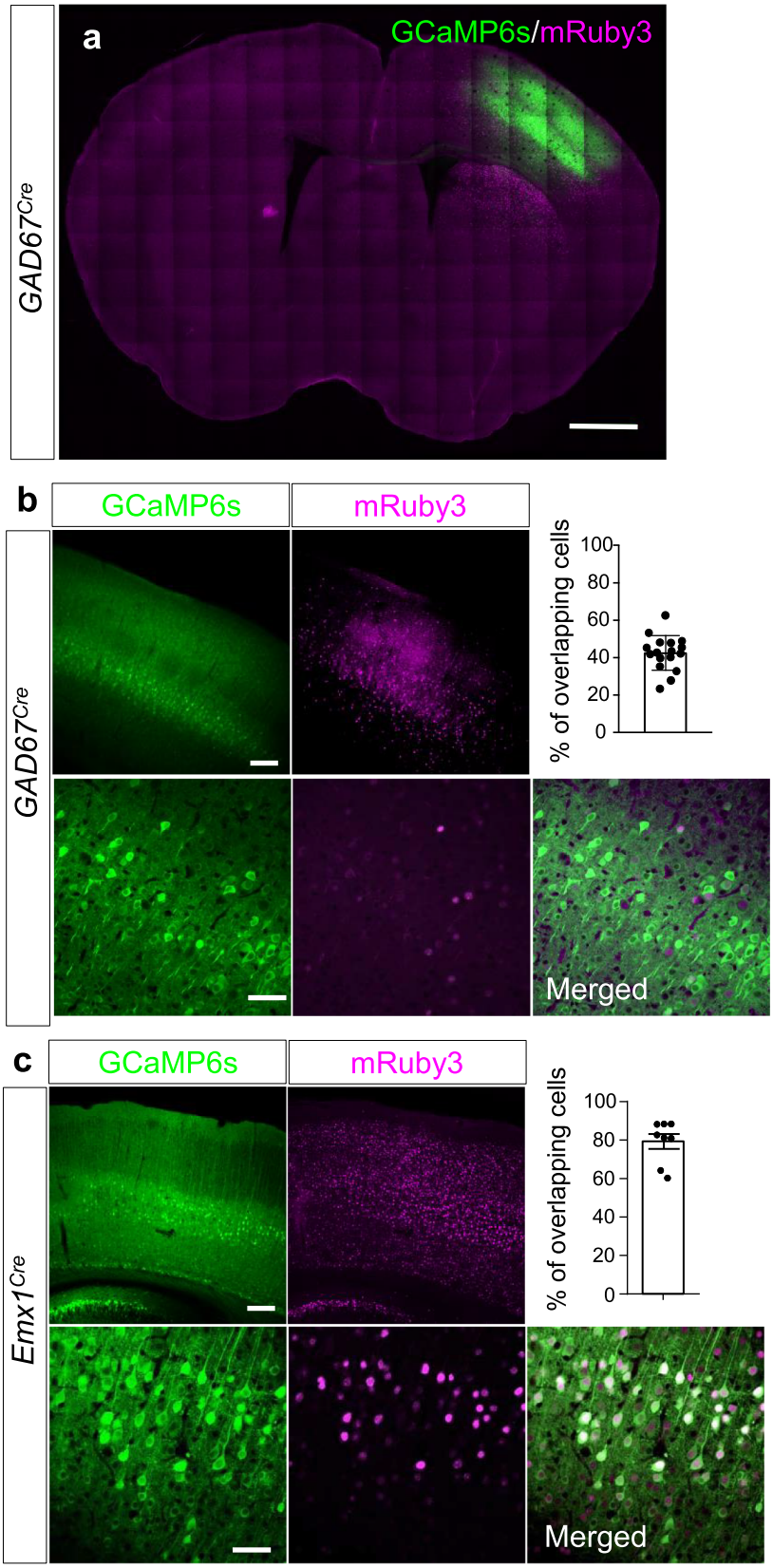

Extended Data Fig. 4 | a, Representative photomicrograph showing AAV1.hSyn.GCaMP6s and AAV9.CAG.DIO.ChroME-ST.mRuby3 injections spread at P8, in GAD67Cre/+ mice (sections at 70 µm). Scale bar: 1 mm. **b**, Representative example and detail of AAVs infection in a GAD67Cre/+ pup injected at birth (sections at 70 µm). Scale bar: 100 µm and 50 µm. Quantification of the fraction of cells expressing ChroME and GCaMP6s. Only 41 ± 5% of the cells expressing ChroME (mRuby3) also expressed GCaMP6s (n = 5 pups (3 females and 2 males), 17 FOVs). **c**, Representative example and detail of AAVs infection in a representative Emx1 Cre pup injected at birth (sections at 70 µm). Scale bar :100 µm and 50 µm. Quantification of the fraction of cells expressing ChroME and GCaMP6s. 80 ± 4% of the cells expressing ChroME (mRuby3) expressed GCaMP6s (n = 3 pups (2 females and 1 male), 8 FOVs). Each dot represents an imaging session. Data are given as mean ± SEM.

https://doi.org/10.1038/s41593-023-01405-5

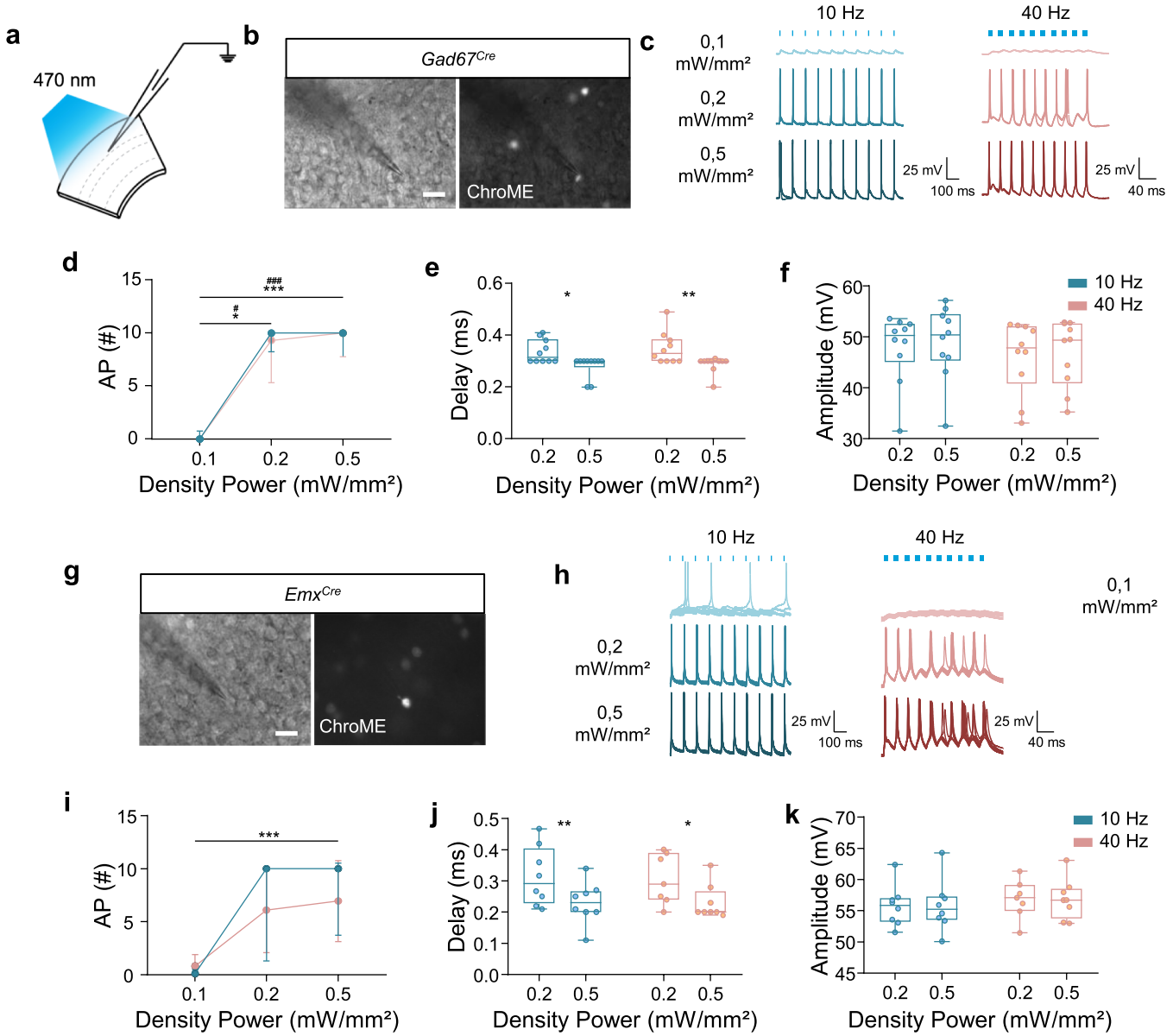

Extended data Fig. 5 | a, Schematic representation of the photostimulation protocol (blue light, 470 nm) used in slices of L2/3 barrel cortex (p7-9). Scale bar 20 µm **b**, Patched ChroME-expressing cell from a GAD67Cre mouse pup injected with AAV9.CAG.DIO.ChroME-ST.mRuby3 at birth (n = 10 cells, 4 pups, 3 females and 1 male). **c**, Representative spikes evoked, in ChroME-expressing GABA cells, by trains of 0.1, 0.2, and 0.5 mW/mm2 light pulses delivered at 10 (blue) and 40 Hz (pink). **d**, Number of action potentials (AP) in ChroME-expressing GABA cells during 10 (blue) and 40 Hz (pink) light stimulation trains as a function of LED power. Two-sided Friedman test: $p < 0.0001$. Dunn's post hoc comparison indicates differences at 10 Hz between 0.1 vs. 0.2 ($p = 0.015$) and 0.1 vs. 0.5 ($p = 0.0003$) and differences at 40 Hz between 0.1 vs. 0.2 ($p = 0.0304$) and 0.1 vs. 0.5 ($p = 0.0001$) at 40 Hz. **e**, Delay measured in ChroME-expressing GABA cells for 10 (blue) and 40 Hz (pink) light stimulation trains at 0.2 and 0.5 mW/mm2. Wilcoxon (two-sided) test ($p = 0.015$, $p = 0.007$). **f**, Spike amplitude measured in ChroME-expressing GABA cells for 10 and 40 Hz stimulation trains at 0.2 and 0.5 mW/mm2. **g**, Patched ChroME-expressing cell from a Emx1 Cre/+ mouse pup injected with AAV9.CAG.DIO.ChroME-ST.mRuby3 at birth (n = 8 cells, 5 pups, 3 females and 2 males). Scale bar 20 µm. **h**, Representative spikes evoked, in ChroME-expressing glutamatergic cells, by trains of 0.1, 0.2, and 0.5 mW/mm2 light pulses delivered 10 (blue traces) and 40 Hz (pink traces). **i**, Number of AP in ChroME-expressing glutamatergic cells during 10 (blue) and 40 Hz (pink) light stimulation trains as a function of LED density power. Two-sided Friedman test: $p < 0.0001$. Dunn's post hoc comparison indicates differences at 10 and 40 Hz between 0.1 vs. 0.5 ($p = 0.0009$) **j**, Delay measured in ChroME-expressing glutamatergic cells for 10 (blue) and 40 Hz (pink) light stimulation trains at 0.2 and 0.5 mW/mm2. Wilcoxon test (10 Hz, $p = 0.015$, 40 Hz, $p = 0.007$). **k**, Spike amplitude measured in ChroME- expressing glutamatergic cells for 10 and 40 Hz stimulation trains at 0.2 and 0.5 mW/mm^2. Each dot represents a cell. Data in panels d and I is given as mean and −/+SEM. Data in panels e, f, j, and k are given as median and interquartile range.

https://doi.org/10.1038/s41593-023-01405-5

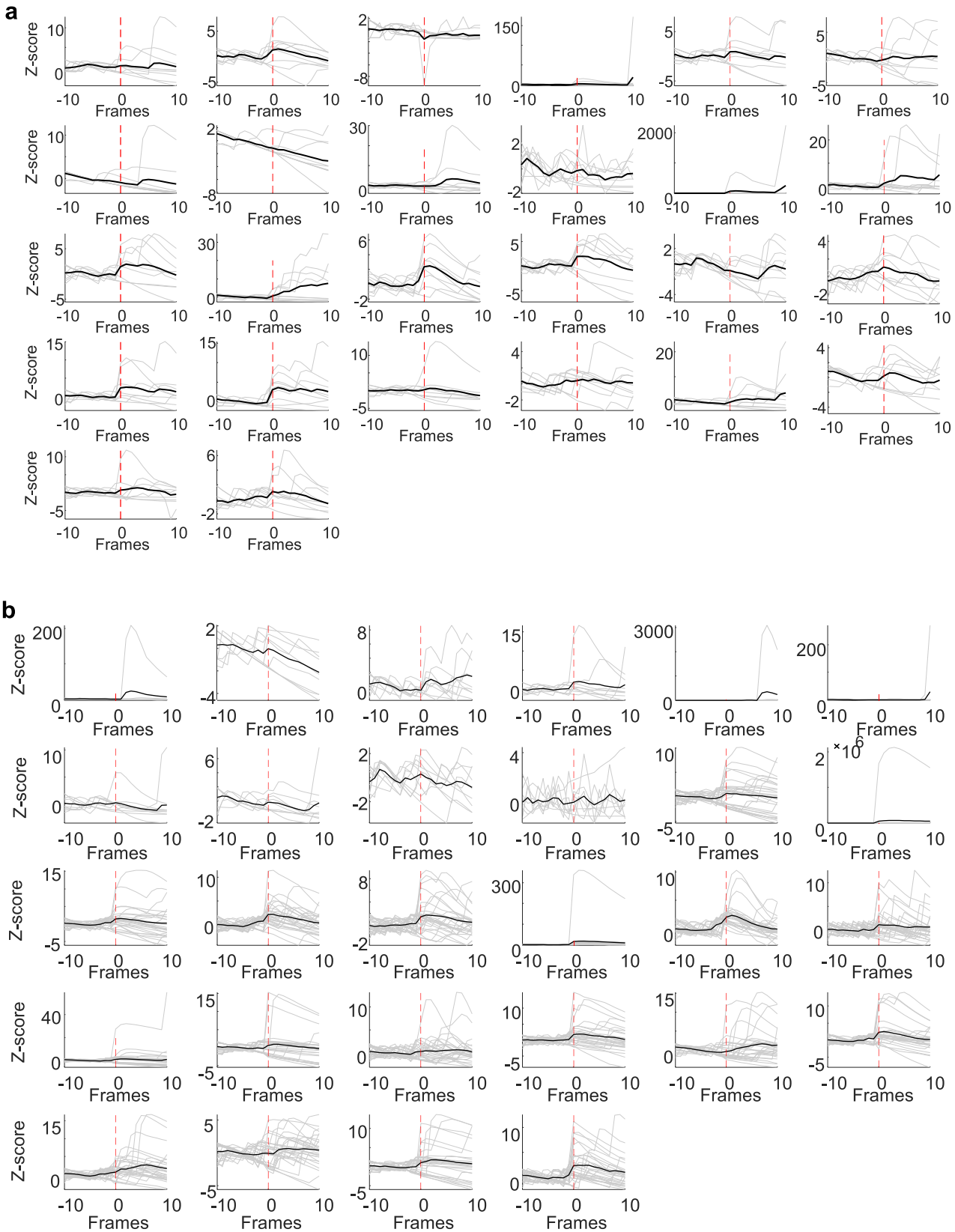

Extended Data Fig. 6 | a, GABA cells response to holographic stimulation. DF/F cell responses to light pulses. Panels indicate the cell response to holographic stimulation (n = 26 GABAergic cells). Grey lines correspond to a single response and black lines correspond to the averaged cell response. Each panel correspond to a single GABA cell stimulated. Responses were normalized by the pooled mean and standard deviation of the baseline (10 frames before stimulation started). **b**, Glutamatergic cells response to holographic stimulation. DF/F cell responses to light pulses. Panels indicate the cell response to holographic stimulation (n = 28 Glutamatergic cells). Grey lines correspond to a single response and black lines correspond to the averaged cell response. Each panel correspond to a single glutamatergic cell stimulated. Responses were normalized by the pooled mean and standard deviation of the baseline (10 frames before stimulation started).

https://doi.org/10.1038/s41593-023-01405-5

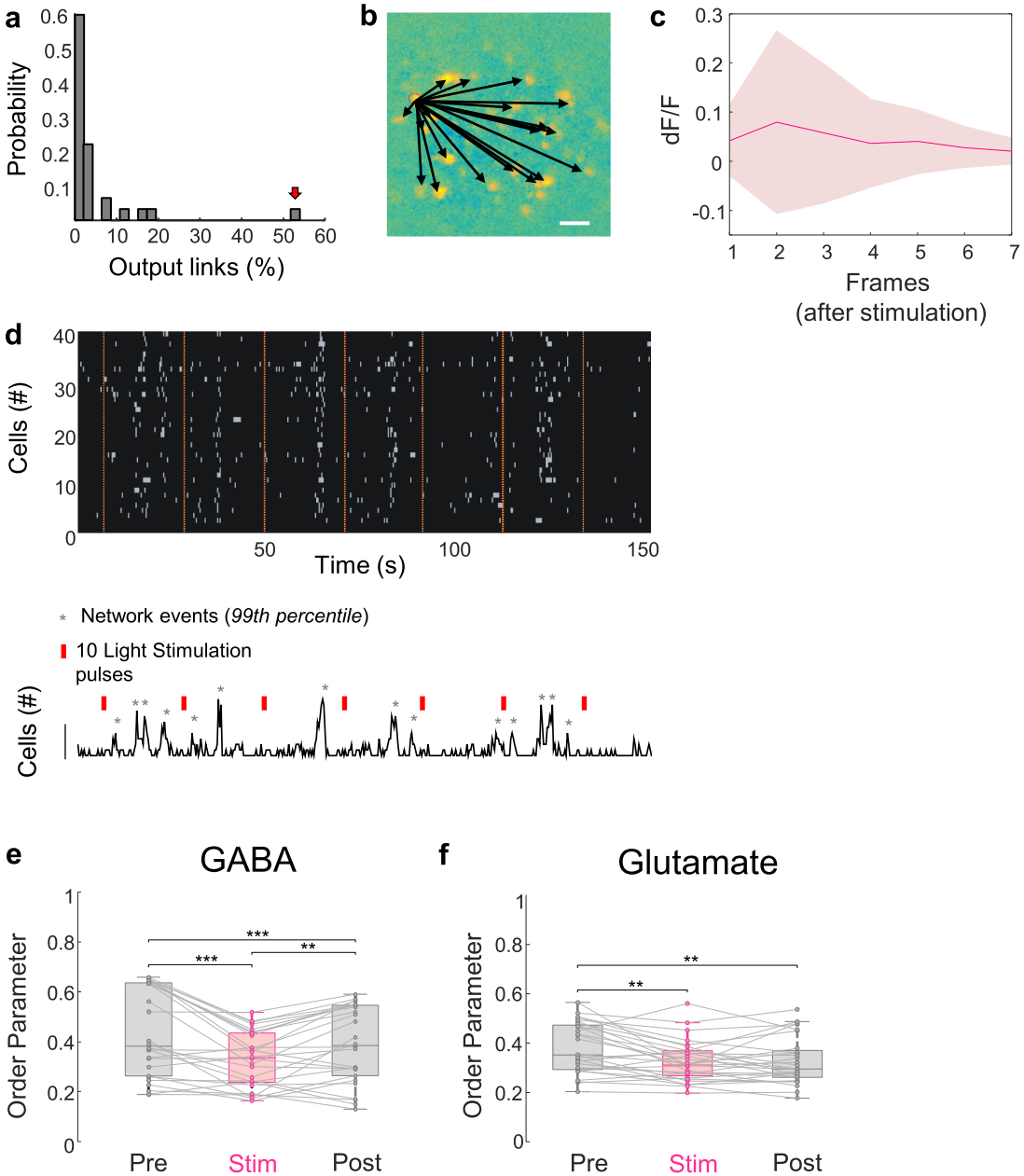

Extended Data Fig. 7 | Light pulses do not induce changes in network activity. **a**–**d**. Example of a HC GCaMP6s positive and ChroME-ST negative stimulated cell. **a**, Probability distribution of cells functional output links (%). Red arrow indicates the output link connectivity of the stimulated cell. **b**, Correlation image of an imaging session and functional output links of the stimulated cell. **c**, Averaged fluorescent calcium event triggered in response to photostimulation (10 pulses, 10hz, 10 ms). Shadow indicates SEM. Data is given as Mean and −/+ SEM **d**, Raster plot of active cells and stimulation pulses. Grey stars indicate detected network events. Scale 5 cells. **e** & **f**, Changes in the median order parameter between Baseline, Stimulation (Stim) and Post-Stimulation (Post) for all stimulated GABA (**e**) (n = 11 pups, 7 females and 4 males, 26 stimulated cells) (two-sided t-test; Pre-Stim: p = 1.13e-4; Pre-Post: p = 8.21e-4; Stim-Post: p = 0.004) and glutamatergic (f) cells (n = 8 pups, 28 stimulated cells) (two-sided t-test; Pre-Stim: p = 0.01; Pre-Post: p = 0.002; Stim-Post: p = 0.71). Each dot represents a FOV. Data are given by Median and interquartile range.

https://doi.org/10.1038/s41593-023-01405-5

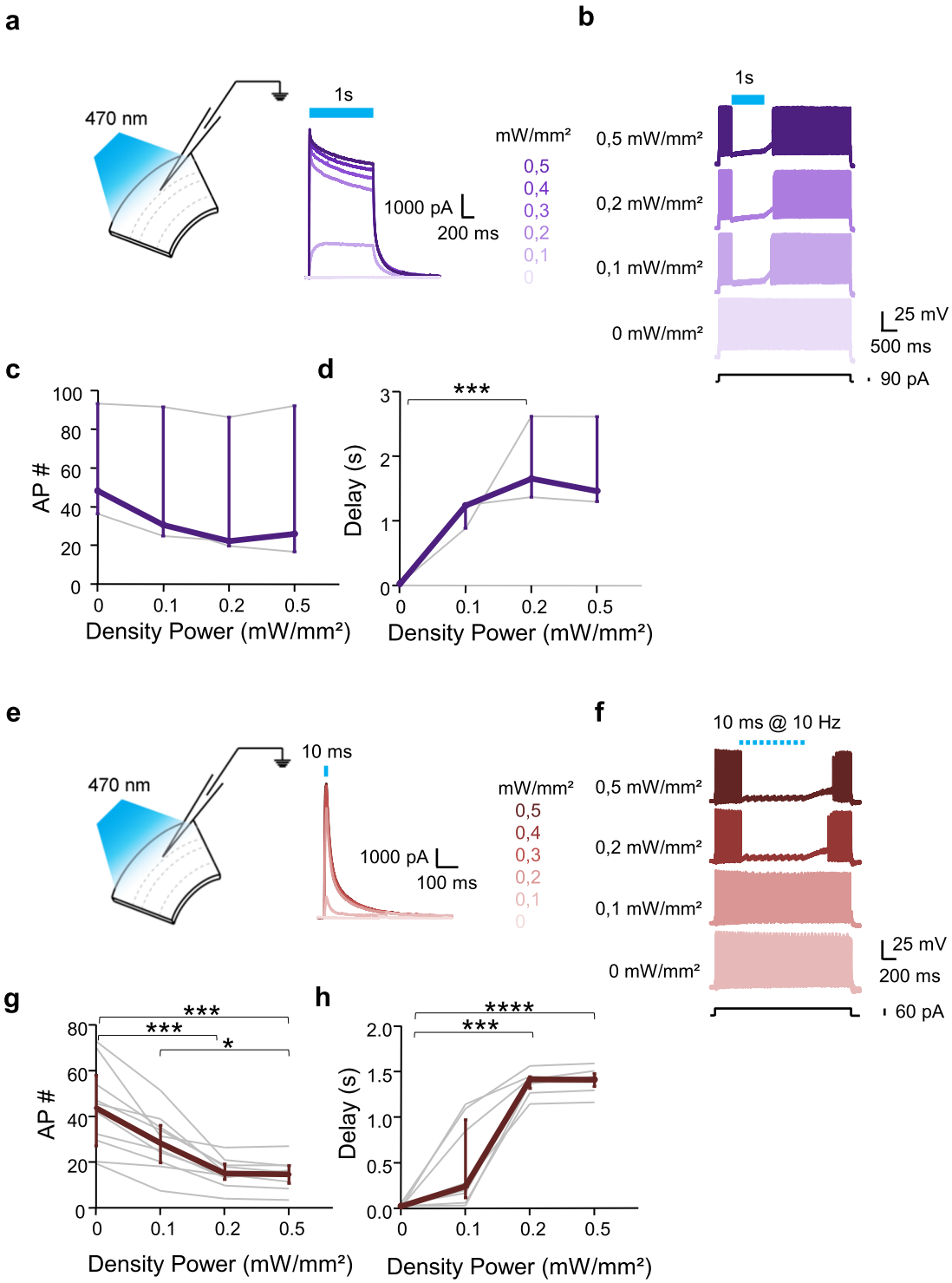

Extended Data Fig. 8 | a and e, Left: Schematic representation of P8–P10 GtACR1-positive cells recorded during photostimulation (blue light, 470 nm) in the L2/3 of S1BF (n = 10 cells, 3 pups, 2 females and 1 male). Right: Photocurrent measured during the stimulation protocol for different LED power (0, 0.1, 0.2, 0.3, 0.4 and 0.5 mW/mm2). **b**, Representative spikes evoked in GtACR1- expressing Lhx6 cells, with a single light pulse (1 s) delivered at 0, 0.1, 0.2, and 0.5 mW/mm^2. **c**, Number of AP in GtACR1-expressing Lhx6 cells during a single pulse (1 s) as a function of LED power. Two-sided Friedman test: $p = 0.07$. **d**, Delay measured from the onset of the light pulse to the following spike in GtACR1-expressing Lhx6 cells during the application of a 1 s light pulse at 0, 0.1, 0.2 and 0.5 mW/mm2. Two-sided Friedman test: $p = 0.001$. Dunn's post hoc comparison indicates differences between 0 vs. 0.2 ($p < 0.05$). **f**, Representative spikes evoked, in GtACR1-expressing Lhx6 cells, by 1 s trains of 0, 0.1, 0.2, and 0.5 mW/mm^2 light pulses (10 ms) delivered at 10 Hz. **g**, Number of AP in GtACR1-expressing Lhx6 cells during 10 Hz light stimulation trains as a function of LED power. Two-sided Friedman test: $p < 0.0001$. Dunn's post hoc comparison indicates differences at 10 Hz between 0 vs. 0.2 ($p = 0.0006$); 0 vs. 0.5 ($p < 0.0001$) and 0.1 vs. 0.5 ($p = 0.014$). **h**, Delay measured from the onset of the light pulse to the following spike in GtACR1-expressing Lhx6 cells during 10 Hz light stimulation trains at 0, 0.1, 0.2 and 0.5 mW/mm2. Friedman test: $p < 0.0001$. Dunn's post hoc comparison indicates differences at 10 Hz between 0 vs. 0.2 ($p = 0.0004$) and 0 vs. 0.5 ($p = 0.0002$). In **c**, **d**, **g** and **h**, each light grey line represents a photoinhibited cell and dark lines represents median and interquartile range.

https://doi.org/10.1038/s41593-023-01405-5

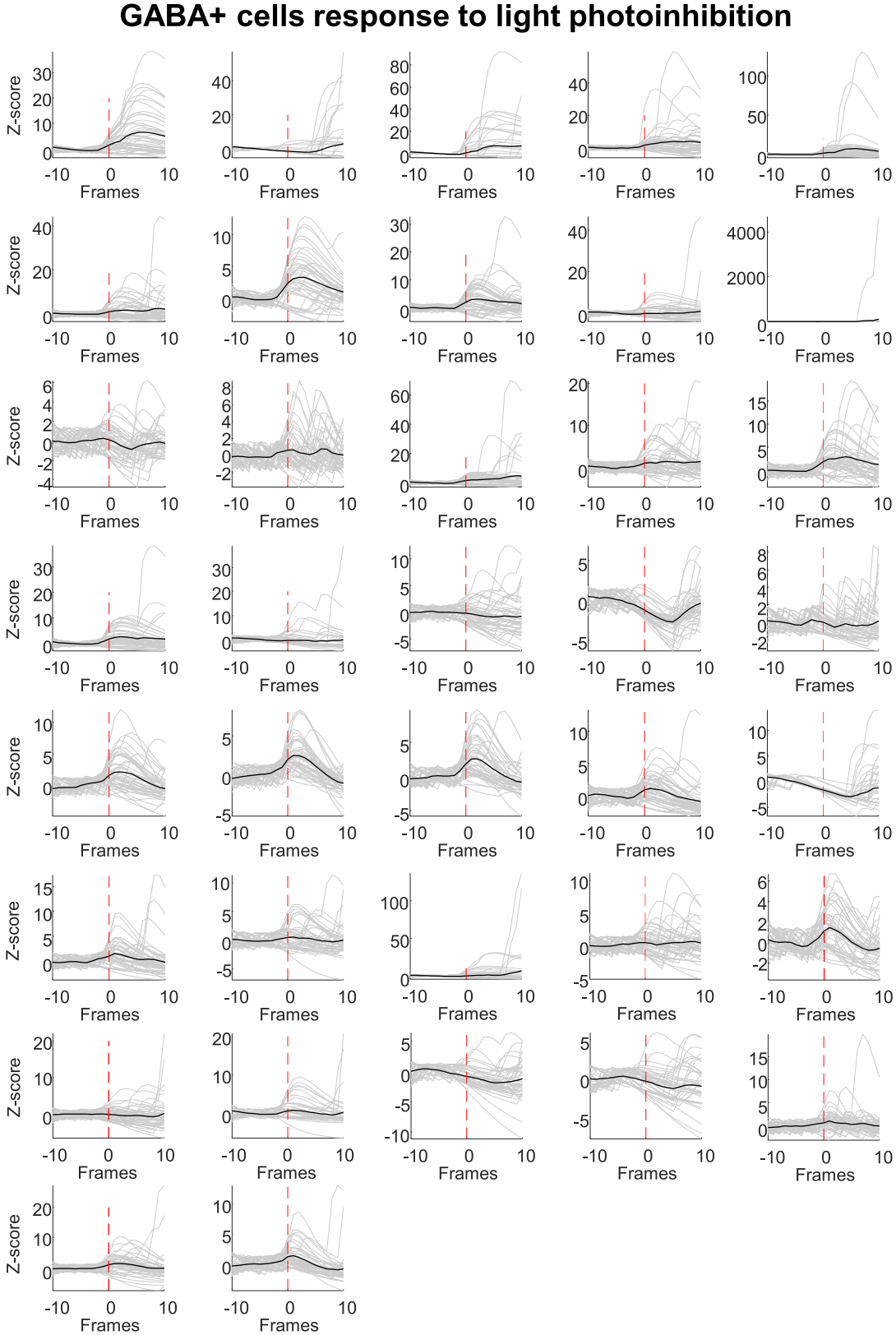

Extended data Fig. 9 | DF/F cell responses to light pulses. Panels indicate the cell response to holographic stimulation (n = 37). Grey lines correspond to a single response and black lines correspond to the averaged cell response. Each panel correspond to a single cell stimulated. Responses were normalized by the pooled mean and standard deviation of the baseline (10 frames before stimulation started). Cells that did not had a time locked response to WS were excluded from the analysis (n = 6 cells).

https://doi.org/10.1038/s41593-023-01405-5

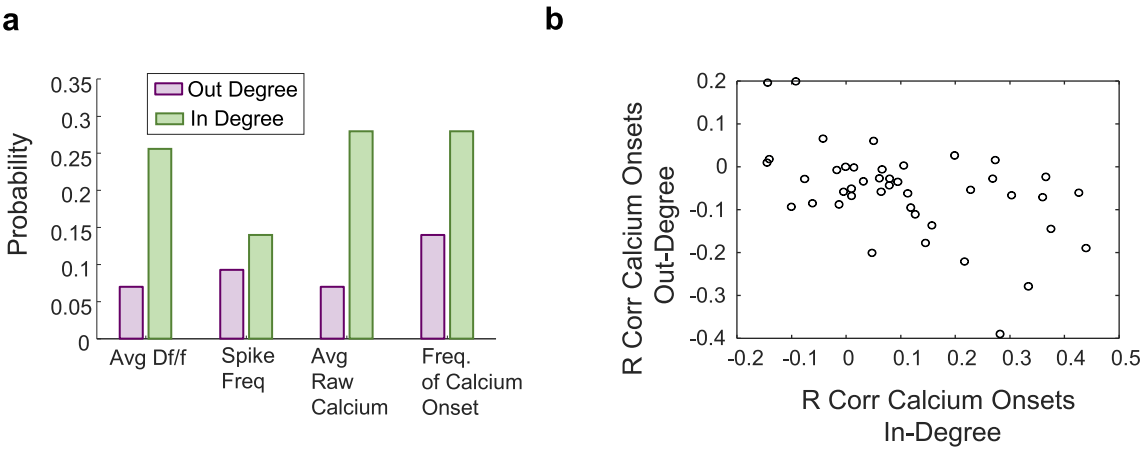

Extended Data Fig. 10 | a, Distribution of the correlation coefficients per FOV of the cells firing activity during WS relative to control (no WS) and the In and Out degree of imaged cells. We used four different measures to characterize activity during calcium imaging (average df/f, spike frequency, average raw calcium traces and frequency of calcium onsets global activity). For all measures we found a significant relationship between differences in calcium activity during control and WS and the connectivity of the imaged cells. The amount of FOVs for which this relationship is significant is higher for In than Out degree. **b**, Correlation plot indicating that the cells with a high correlation coefficient between In degree and the cell firing within WS (Two-sided t-test: $p < 0.001$), display lower correlation with their Out degree.

QUERY FORM

Manuscript ID	**[Art. Id: 1405]**
Author	**Yannick Bollmann**

AUTHOR:

The following queries have arisen during the editing of your manuscript. Please answer by making the requisite corrections directly in the e.proofing tool rather than marking them up on the PDF. This will ensure that your corrections are incorporated accurately and that your paper is published as quickly as possible.

Query No.	*Nature of Query*
Q1:	Please check your article carefully, coordinate with any co-authors and enter all final edits clearly in the eproof, remembering to save frequently. Once corrections are submitted, we cannot routinely make further changes to the article.
Q2:	Note that the eproof should be amended in only one browser window at any one time; otherwise changes will be overwritten.
Q3:	Author surnames have been highlighted. Please check these carefully and adjust if the first name or surname is marked up incorrectly. Note that changes here will affect indexing of your article in public repositories such as PubMed. Also, carefully check the spelling and numbering of all author names and affiliations, and the corresponding email address(es).
Q4:	You cannot alter accepted Supplementary Information files except for critical changes to scientific content. If you do resupply any files, please also provide a brief (but complete) list of changes. If these are not considered scientific changes, any altered Supplementary files will not be used, only the originally accepted version will be published.
Q5:	Please check Figures for accuracy as they have been relabelled. Please markup minor changes in the eProof. For major changes, please provide revised figures. (Please note that in the eProof the figure resolution will appear at lower resolution than in the pdf and html versions of your paper.)
Q6:	If applicable, please ensure that any accession codes and datasets whose DOIs or other identifiers are mentioned in the paper are scheduled for public release as soon as possible, we recommend within a few days of submitting your proof, and update the database record with publication details from this article once available.
Q7:	Please check the edits here: "Spontaneous synchronous activity is a universal process by which developing neuronal networks adjust their cell numbers, mature single-cell morpho-physiological properties and form and prune synapses[1,2]."
Q8:	Your paper has been copyedited. Please review every sentence to ensure that it conveys your intended meaning; if changes are required, please provide further clarification rather than reverting to the original text. Please note that formatting (including hyphenation, Latin words, and any

QUERY FORM

Manuscript ID	**[Art. Id: 1405]**
Author	**Yannick Bollmann**

AUTHOR:

The following queries have arisen during the editing of your manuscript. Please answer by making the requisite corrections directly in the e.proofing tool rather than marking them up on the PDF. This will ensure that your corrections are incorporated accurately and that your paper is published as quickly as possible.

Query No.	*Nature of Query*
	reference citations that might be mistaken for exponents) has been made consistent with our house style.
Q9:	Please ensure that genes are correctly distinguished from gene products: for genes, official gene symbols (e.g., NCBI Gene) for the relevant species should be used and italicized; gene products such as proteins and noncoding RNAs should not be italicized. Please check the figures, too.
Q10:	Please note, we reserve 'significant' and its derivatives for statistical significance. Please review the use of 'significant' or 'significantly' throughout this paper and change to 'substantial', 'considerable', or 'important' or their derivatives if appropriate.
Q11:	We conform to the style that vectors are set in bold roman font. The magnitude of a vector is set in nonbold italics, as are scalar components, tensors and matrices. Please ensure your text is consistent with this throughout.
Q12:	Please check the edits here: "...by crossing *GAD67Cre/+* with the reporter line *Ai96*..."
Q13:	Please check the edits here: "...highest input connectivity within a given age group), which were connected to..."
Q14:	Please check the edits here: "Hence, the fraction of HC_{global_out} and HC_{global_in}cells significantly increased..."
Q15:	Please check the edits here: "Contour map of all active cells with the targeted HC GABAergic (**a** 2) and glutamatergic (**b** 2) cell (pink) and arrows indicating its functional (outputs and input) links."
Q16:	Please check the edits here: "...imaging lasers below 5 mV^{31}."
Q17:	Please check the edits here: "Targeted ST-GtACR1-expressing cells displayed a significant decrease in calcium transients time-locked to the photoinhibition protocol using both in vitro current-clamp recordings in *Lhx6Cre/+*ST-GtACR1-expressing cells (Extended Data Fig. 8) and in vivo two-photon holographic inhibition (continuous suppression of activity for five frames

QUERY FORM

Manuscript ID	**[Art. Id: 1405]**
Author	**Yannick Bollmann**

AUTHOR:

The following queries have arisen during the editing of your manuscript. Please answer by making the requisite corrections directly in the e.proofing tool rather than marking them up on the PDF. This will ensure that your corrections are incorporated accurately and that your paper is published as quickly as possible.

Query No.	*Nature of Query*
	locked to the whisker stimulation (WS) 0.3-0.5 mW μm^{-2}, on a spot size of 10 µm) (Methods and Extended Data Fig. 9)."
Q18:	Please check the edits here: "**a**, Schematic representation of the experimental paradigm. Photoinhibition experiments and imaging sessions..."
Q19:	Please check the edits here: "The use of a fast opsin also enables, under our imaging conditions, to minimize the excitation crosstalk from the imaging laser for experiments combining functional imaging with optical photostimulation or photoinhibition."
Q20:	Please check the edits here: "Our experiments performed in Lhx6$^{Cre/+}$mice..."
Q21:	Please note that reference [63] was cited in the article, but has not been included in the reference list. Please supply details for the missing reference.
Q22:	Please indicate what the '63' represents: "No developmental abnormalities or aberrant activity was observed in *GAD67Cre/+;Ai9663*."
Q23:	Please check these sentences and ensure that they reflect your intended meaning, specifically the placement of the number '21'. In one place, '21' is used as a reference citation; in another, it's the number of mice. "We used double heterozygous GAD67Cre/+ mice21 crossed with Ai14 [B6;129S6-Gt(ROSA)26Sortm14(CAG-tdTomato)Hze/J] (n = 17) or RCL-GCaMP6s (Ai96) [B6;129S6-Gt(ROSA)26Sortm96.1(CAG-GCaMP6s)Hze/J] (The Jackson Laboratory) (n = 10) for calcium imaging experiments in vivo (including four pups for the sensory deprivation experiments). GAD67Cre/+21 and Emx1Cre/+ (The Jackson Laboratory) mice were used for imaging combined to holographic stimulation experiments in vivo and 21 (Emx1Cre/+ n = 10 and GAD67Cre n = 11 pups) and in vitro (n = 7 in total)."
Q24:	I'm not sure what this means. Please clarify: "...f = LJ1558L1-B, Thorlabs..."
Q25:	I'm not sure what 'Vincent' means. Please clarify: "...Vincent Sutter Instrument..."
Q26:	Please check the edits here: " We then calculated $\Delta C_{norm}/\Delta t$..."

QUERY FORM

Manuscript ID	**[Art. Id: 1405]**
Author	**Yannick Bollmann**

AUTHOR:

The following queries have arisen during the editing of your manuscript. Please answer by making the requisite corrections directly in the e.proofing tool rather than marking them up on the PDF. This will ensure that your corrections are incorporated accurately and that your paper is published as quickly as possible.

Query No.	*Nature of Query*
Q27:	Please check that all funders have been appropriately acknowledged and that all grant numbers are correct.
Q28:	If applicable, please ensure accession codes are scheduled for release on or before this article's scheduled publication date and update the database record with publication details from this article once available.
Q29:	Please check that the Competing Interests declaration is correct as stated. If you declare competing interests, please check the full text of the declaration for accuracy and completeness.

nature portfolio

Corresponding author(s): Dr. Rosa Cossart

Last updated by author(s): 26/6/23

Reporting Summary

Nature Portfolio wishes to improve the reproducibility of the work that we publish. This form provides structure for consistency and transparency in reporting. For further information on Nature Portfolio policies, see our Editorial Policies and the Editorial Policy Checklist.

Statistics

For all statistical analyses, confirm that the following items are present in the figure legend, table legend, main text, or Methods section.

n/a	Confirmed
☐	☒ The exact sample size (*n*) for each experimental group/condition, given as a discrete number and unit of measurement
☐	☒ A statement on whether measurements were taken from distinct samples or whether the same sample was measured repeatedly
☐	☒ The statistical test(s) used AND whether they are one- or two-sided *Only common tests should be described solely by name; describe more complex techniques in the Methods section.*
☒	☐ A description of all covariates tested
☐	☒ A description of any assumptions or corrections, such as tests of normality and adjustment for multiple comparisons
☐	☒ A full description of the statistical parameters including central tendency (e.g. means) or other basic estimates (e.g. regression coefficient) AND variation (e.g. standard deviation) or associated estimates of uncertainty (e.g. confidence intervals)
☐	☒ For null hypothesis testing, the test statistic (e.g. *F*, *t*, *r*) with confidence intervals, effect sizes, degrees of freedom and *P* value noted *Give P values as exact values whenever suitable.*
☒	☐ For Bayesian analysis, information on the choice of priors and Markov chain Monte Carlo settings
☒	☐ For hierarchical and complex designs, identification of the appropriate level for tests and full reporting of outcomes
☒	☐ Estimates of effect sizes (e.g. Cohen's *d*, Pearson's *r*), indicating how they were calculated

Our web collection on statistics for biologists contains articles on many of the points above.

Software and code

Policy information about availability of computer code

Data collection

In vivo two-photon calcium imaging:
Imaging was performed with a single beam multiphoton-pulsed laser scanning system coupled to a microscope (TriM Scope II, LaVision Biotech, Bielefeld, DE). The Ti: sapphire excitation laser (Chameleon Ultra II, Coherent) was operated at 920 nm with a maximum 35mW power under the objective lens. GCaMP fluorescence was isolated using a bandpass filter (510/25). Images were acquired through a GaAsP PMT (H7422-40, Hamamatsu) using a 16X immersion objective (NIKON, NA 0.8). Using Imspector software 5.0.164 (LaVision Biotech, Bielefeld, DE), the fluorescence signal from a 600X600 µm2 field of view was acquired at 1.5 or 2.7Hz with respectively 2,54 µs or 1,2 µs dwell time per pixel (1,17 µm/pixel).

In vivo two-photon calcium imaging and holographic stimulation:
The optical system was a custom-built microscope combining galvo-based two-photon scanning with Computer Generated Holography. Raster scanning of calcium fluorescence signals was achieved using standard galvo scanners and a pulsed femtosecond imaging LASER source. The LASER beam (Chameleon Ultra II, Coherent) was expanded with two lenses telescope assembly (f = 300 mm, f = 500 mm) and projected onto a XY galvo mirror pair (6215H, Cambridge Technology) controlled with two servo driver cards (67125H-1HP-FS60, Cambridge Technology). A half-wave plate (#AWHP10M-980, Thorlabs) and a polarizer (#GT10-B, Thorlabs) were used to adjust LASER power. Next, a scan and a tube lens (focal length fS = 50 mm and fT = 375 mm, respectively) were used to conjugate the XY scanner focal plane to the back focal plane of the microscope objective (16x Nikon, N.A 0.8). This configuration allowed scanning a field of view of 350 µm * 350 µm (512 pixels * 512 pixels) at the focal plane of the objective with a frame rate of 2.7Hz and a power of 25mW at 920 nm wavelength. To collect the emitted fluorescent signal, the back focal plane of the objective and the focal plane of a GaAsP PMT (Hamamatsu, H7244-20) were conjugated through a relay of lenses (f = 100 mm, #AC254-100-A, Thorlabs, f = 25 mm, #LA1951-A, Thorlabs). Two spectral filters were mounted in front of the PMT (FF01-770/SP-25, Semrock, ET520/40m, Chroma) to optimize GFP detection. The analog signal was next converted from current to voltage and amplified through a transimpedance amplifier (#TIA60, Thorlabs). Finally, an electronic card (NI6356, National instruments) in

combination with Scanimage software (Vidriotechnologies) was used to control the scanners and to digitalize the analog signal from the PMT. Photostimulation of neurons of interest used Computer Generated Holography. Briefly, the beam of the pulsed femtosecond photoactivation LASER (GOJI, AMPLITUDE SYSTEMS, 10MHz repetition rate, 1030nm) was shaped by a Spatial Light Modulator (Hamamatsu, LCOS-SLM X13138-07). The size of the LASER beam was expanded using a two-lenses telescope assembly (#AC254-030-B, Thorlabs, #AC254-150-B, Thorlabs) so that it covered the entire surface of the SLM. A half-wave plate (#AHWP10M-980, Thorlabs) was used to align the polarization of the laser to the orientation of the liquid crystals. Three lenses (#AC508-300-B) combined with the tube lens (fT = 375 mm) in 4-f configuration enabled conjugating the SLM focal plane to the back focal plane of the microscope objective. The zero-order of the SLM was suppressed with a cylindrical lens (f = 300 mm, f = #LJ1558L1-B, Thorlabs) as described previously. A custom software (Wavefront Designer IV) based on the Gerchberg & Saxton algorithm, was used to convert the photostimulation intensity pattern at the focal plane into a photostimulation phase mask addressed to the SLM.
To combine the two imaging and photostimulation paths, a dichroic mirror (#DMPSP1000L, Thorlabs) was placed at the focal plane of the scan lens. The custom software mentioned above was used to adjust the spatial overlap of the photostimulation pattern with the imaging at 920 nm thanks to a rhodamine fluorescent sample that was bleached at 1030 nm and imaged at 920 nm. To synchronize the paths, a Matlab script defined a photostimulation temporal gate and sent a TTL signal, via the NI card described above, to an obturator (Vincent shutter instruments) placed in front of the photostimulation LASER source during the raster scanning for calcium imaging. Holographic stimulation of targeted cells was achieved with an excitation spot of 10 um lateral size, corresponding to an axial resolution of 20um. Trains of 10 consecutive pulses (10ms duration, at 10 or 40 Hz, at 0.3-0.8 mW/um2 power), were applied every 10 seconds during the stimulation period.

In vitro patch clamp recordings and optogenetics:
Coronal slices (300 µm thick) were obtained from GAD67Cre, Emx1Cre or Lhx6Cre between p7 and p10 in pups injected at birth with AAV9.CAG.DIO.ChroME-ST.mRuby3 or with AAV9.CAG.nls.mRuby2.IRES.GtACR1casac, using a Leica VT1200 S vibratome in ice-cold oxygenated modified artificial cerebrospinal fluid (in nM): 2.5 KCl, 1.25 NaH2PO4, 7 MgCl2, 5 CaCl2, 26 NaHCO3, 5 D-glucose, 126 CholineCl. Slices were then kept for rest (1 hr, room temperature) in oxygenated normal ACSF containing (in mM): 126 NaCl, 3.5 KCl, 1.2 NaH2PO4, 26 NaHCO3, 1.3 MgCl2, 2.0 CaCl2, and 10 D-glucose. Patch clamp recordings were carried out using a SliceScope Pro 1000 rig (Scientifica) equipped with a CCD camera (Hamamatsu Orca-05G). Slices were transferred to a submerged recording chamber and continuously perfused with oxygenated ACSF (3 mL/min) at ~32°C. Electrodes (4-8 MΩ resistance) were pulled using a PC-10 puller (Narishige) from borosilicate glass capillaries (GC150F-10, Harvard Apparatus) and filled with a filtered current clamp intracellular solution containing (in mM): 125 K-methylSO4, 15 KCl, 5 NaCl, 10 HEPES, 2.5 Mg-ATP, 0.3 Na-GTP (pH 7.3 and ~280 mOsm). Electrophysiological signals were amplified (Multiclamp 700B), low-pass filtered at 2.9 kHz, digitized at 10 kHz and acquired using a Digidata 1440A digitizer and pClamp 10 software (all from Molecular Devices). An optoLED system (Cairn Research) consisting of two 3.5W LEDs was used to visualize fluorescence signals and stimulate ChroME- or GtACR1-expressing neurons in S1BF. A 470 nm LED coupled to a GFP filter cube was used to activate ChroME- or GtACR1-expressing neurons (ChroME: 10 ms per pulses; GtACR1: 10 ms or 1 s per pulses). A white LED coupled to an RFP filter cube was used to visualize ChroME/mRuby- or GtACR1/mRuby-expressing neurons. Light was delivered using a 40× objective, leading to an illumination field of ~1 mm2. For ChroMe-expressing neuron stimulation, spikes were evoked by trains of 10 pulses (10 ms at 10 or 40Hz) at different intensity power (0.1, 0.2, and 0.5 mW/mm²). The response delay, the number of spikes and their amplitude were measured with Clampfit 10.7 (Molecular Devices). For GtACR1-expressing neuron stimulation, the photocurrent evoked by a 1-second or 10-ms light pulse was measured. Two protocols were used to observe the effect of GtACR1 stimulation when neurons fired : (1) a 1-second continuous light pulse at different intensity power (0.1, 0.2, and 0.5 mW/mm²) applied simultaneously to a 4-second suprathreshold depolarising step, (2) a train of 10 light pulses (10-ms at 10 Hz) at different intensity power (0.1, 0.2, and 0.5 mW/mm²) applied to inhibit spikes triggered by an 1 second suprasubthreshold depolarising step. The number of spikes during the depolarising step and the delay between the last spike before the light pulses and the following spike were measured with Clampfit 10.7.

Data analysis

Software used for data analysis:
MATLAB, R, Graphpad Prism 7 & 9. All custom-made codes to analyze the calcium data are available at: https://gitlab.com/cossartlab/holohub
Other publicly available packages used for data analysis:
CaImAn: Pnevmatikakis et al., 2016; Giovannucci et al., 2018, https://github.com/flatironinstitute/CaImAn-MATLAB
NoRMCorre: Pnevmatikakis and Giovannucci, 2017, https://github.com/flatironinstitute/NoRMCorre
poweRlaw package: Clauset et al, 2009, Gillespie, C. S, 2015, https://github.com/csgillespie/poweRlaw
CASCADE, Rupprecht et al, 2021, https://github.com/HelmchenLabSoftware/Cascade
Brain Connectivity Toolbox: Rubinov and Sporns, 2010, https://sites.google.com/site/bctnet/

For manuscripts utilizing custom algorithms or software that are central to the research but not yet described in published literature, software must be made available to editors and reviewers. We strongly encourage code deposition in a community repository (e.g. GitHub). See the Nature Portfolio guidelines for submitting code & software for further information.

Data

Policy information about availability of data

All manuscripts must include a data availability statement. This statement should provide the following information, where applicable:

- Accession codes, unique identifiers, or web links for publicly available datasets
- A description of any restrictions on data availability
- For clinical datasets or third party data, please ensure that the statement adheres to our policy

All custom-made codes to analyze calcium imaging data and the data are available here: https://gitlab.com/cossartlab/holohub
All data supporting the findings of this study are available from https://gitlab.com/cossartlab/

Research involving human participants, their data, or biological material

Policy information about studies with human participants or human data. See also policy information about sex, gender (identity/presentation), and sexual orientation and race, ethnicity and racism.

Reporting on sex and gender: N/A

Reporting on race, ethnicity, or other socially relevant groupings	N/A
Population characteristics	N/A
Recruitment	N/A
Ethics oversight	N/A

Note that full information on the approval of the study protocol must also be provided in the manuscript.

Field-specific reporting

Please select the one below that is the best fit for your research. If you are not sure, read the appropriate sections before making your selection.

☒ Life sciences ☐ Behavioural & social sciences ☐ Ecological, evolutionary & environmental sciences

For a reference copy of the document with all sections, see nature.com/documents/nr-reporting-summary-flat.pdf

Life sciences study design

All studies must disclose on these points even when the disclosure is negative.

Sample size	The number of sample size (N) is reported in the figure legends or in the text. No statistical methods were used to predetermine sample size, but sample size was chosen based on previous studies (Modol et al., 2020; Modol et al., 2017; Picardo et al., 2011; Bonifazi et al., 2009) and taking in consideration the three Rs principle.
Data exclusions	All recordings with no technical issues were included in the analysis. Animals without sufficient calcium indicator or opsin expression (i.e ST-ChroME or ST-GtACR1) were excluded because functional imaging could not be efficiently performed in those pups.
Replication	The experiments reported in this work were replicated successfully in a new experimental data set that we included in the final version of this study. These experiments were performed by different experimentalists. Therefore, results were replicated twice by two different groups of experimentalists.
Randomization	Randomization in this study was performed using animals from different sex and litters. Additionally, in vivo experiments were performed at different day times. None of the mentioned randomization measures had an impact on the results obtained.
Blinding	Blinding was not possible because the same researchers collected and analyzed the in vivo calcium imaging data.

Reporting for specific materials, systems and methods

We require information from authors about some types of materials, experimental systems and methods used in many studies. Here, indicate whether each material, system or method listed is relevant to your study. If you are not sure if a list item applies to your research, read the appropriate section before selecting a response.

Materials & experimental systems

n/a	Involved in the study
☒	☐ Antibodies
☒	☐ Eukaryotic cell lines
☒	☐ Palaeontology and archaeology
☐	☒ Animals and other organisms
☒	☐ Clinical data
☒	☐ Dual use research of concern
☒	☐ Plants

Methods

n/a	Involved in the study
☒	☐ ChIP-seq
☒	☐ Flow cytometry
☒	☐ MRI-based neuroimaging

Animals and other research organisms

Policy information about studies involving animals; ARRIVE guidelines recommended for reporting animal research, and Sex and Gender in Research

Laboratory animals	Ai14 (B6;129S6-Gt(ROSA)26Sortm14(CAG-tdTomato)Hze/J (#007914)), Ai96 (B6;129S6-Gt(ROSA)26Sortm96(CAG-GCaMP6s)Hze/J, (#024106), Emx1Cre (B6.129S2-Emx1tm1(cre)Krj/J, (#005628) and LHX6Cre (B6; CBA-Tg(Lhx6-icre)1Kess/J (#026555) were purchased from Jackson Laboratories (Bar-Harbor, USA). The Gad67Cre was a gift from Prof. H. Monyer (Heidelberg University). All animals were used between postnatal day 7 and postnatal day 11.

	All adult mice (breeders) were housed in groups and kept on a 12 h light/dark cycle with ad libitum access to food and water. All mice were bred in a temperature-controlled room at 21°C and 55% humidity. Only time-mated pregnant female mice were housed individually. Male and female mice were used to perform the experiments. in all experiments.
Wild animals	The study did not involved wild animals.
Reporting on sex	Animals (pups) from both sexes were used in this study. No significant differences were observed related to animal' s sex.
Field-collected samples	The study did not involve samples from the field.
Ethics oversight	All animal use protocols were performed under the guidelines of the French National Ethics Committee for Sciences and Health report on ‘‘Ethical Principles for Animal Experimentation’’ in agreement with the European Community Directive 86/609/EEC under agreement APAFIS#18125.

Note that full information on the approval of the study protocol must also be provided in the manuscript.